SANDIA REPORT

SAND2007-8039
Unlimited Release
Printed December 2007

The VELOCE pulsed power generator for isentropic compression experiments

Tommy Ao, James R. Asay, Sophie Chantrenne, Randy J. Hickman, Michael D. Willis, Andrew W. Shay, Suzi A. Grine-Jones, Clint A. Hall, and Melvin R. Baer

Prepared by
Sandia National Laboratories
Albuquerque, New Mexico 87185 and Livermore, California 94550

Sandia is a multiprogram laboratory operated by Sandia Corporation,
a Lockheed Martin Company, for the United States Department of Energy's
National Nuclear Security Administration under Contract DE-AC04-94-AL85000.

Approved for public release; further dissemination unlimited.

Sandia National Laboratories

Issued by Sandia National Laboratories, operated for the United States Department of Energy by Sandia Corporation.

Printed in the United States of America. This report has been reproduced directly from the best available copy.

Available to DOE and DOE contractors from
U.S. Department of Energy
Office of Scientific and Technical Information
P.O. Box 62
Oak Ridge, TN 37831

Telephone:	(865) 576-8401
Facsimile:	(865) 576-5728
E-Mail:	reports@adonis.osti.gov
Online ordering:	http://www.osti.gov/bridge

Available to the public from
U.S. Department of Commerce
National Technical Information Service
5285 Port Royal Rd
Springfield, VA 22161

Telephone:	(800) 553-6847
Facsimile:	(703) 605-6900
E-Mail:	orders@ntis.fedworld.gov
Online ordering:	http://www.ntis.gov/help/ordermethods.asp?loc=7-4-0#online

SAND2007-8039
Unlimited Release
Printed December 2007

The VELOCE pulsed power generator for isentropic compression experiments

Tommy Ao, James R. Asay, Sophie Chantrenne,
Randy J. Hickman, Michael D. Willis, Andrew W. Shay,
Suzi A. Grine-Jones, and Clint A. Hall
Dynamic Material Properties

Melvin R. Baer
Engineering Sciences Center

Sandia National Laboratories
P.O. Box 5800
Albuquerque, NM 87185

Abstract

Veloce is a medium-voltage, high-current, compact pulsed power generator developed for isentropic and shock compression experiments. Because of its increased availability and ease of operation, Veloce is well suited for studying isentropic compression experiments (ICE) in much greater detail than previously allowed with larger pulsed power machines such as the Z accelerator. Since the compact pulsed power technology used for dynamic material experiments has not been previously used, it is necessary to examine several key issues to ensure that accurate results are obtained. In the present experiments, issues such as panel and sample preparation, uniformity of loading, and edge effects were extensively examined. In addition, magnetohydrodynamic (MHD) simulations using the ALEGRA code were performed to interpret the experimental results and to design improved sample/panel configurations. Examples of recent ICE studies on aluminum are presented.

Acknowledgments

The authors would like to thank the companies of ITHPP (International Technologies for High Pulsed Power) and ITI (Ivanhoe Technologies Inc) in constructing the Veloce pulsed power generator, especially Gilles Avrillaud and Mathias Bavay. We wish to acknowledge the collaborative discussions with Washington State University, especially Cory Bakeman. Also, valuable feedback on this work was provided by Marcus Knudson, Jean-Paul Davis, Dan Dolan, Tom Haill, and Wayne Trott.

Contents

List of Figures

List of Tables

Chapter 1

Introduction

Shock wave techniques have been used extensively to collect information on the high-pressure equation-of-state (EOS) of materials [1, 2, 3, 4]. However, most high pressure EOS data have been obtained from shock compression which represents the response of a material along its principal Hugoniot; i.e. the states produced by passage of a steady, single shock wave produced from ambient conditions, or by shock compression of porous samples of the material, which produce higher temperature states at a given compression. The thermodynamic regime below the principal Hugoniot, or cooler states at a given compression, has not been extensively explored in dynamic experiments. Consequently, a significant portion of the complete EOS surface is inadequately understood. The need for accurate off-Hugoniot states measurements has compelled development of several experimental approaches to produce well-controlled continuous, or ramp, loading of condensed matter [5, 6, 7, 8, 9, 10, 11, 12, 13, 14]. The thermodynamic states produced by ramp loading of all materials, and solids in particular, generally produce thermodynamic states close to an isentrope since irreversible effects produced by visco-plastic and plastic work are usually small. This technique is often referred to as Isentropic Compression Experiments, or ICE [15]. In the following, we will use the term quasi-isentropic to refer to the thermodynamic states achieved by ramp loading.

The first efforts to create quasi-isentropic loading employed the impacting of gas gun projectiles onto ramp wave generator buffer materials such as fused silica [5] or pyroceram [6]; this produces shockless loading on target samples mounted on the back surface of the ramp generator. This technique is able to produce loading up to stresses of $\sim$ 20 GPa at most, and is thus limited for materials studies. Further work in developing impact methods for ramp loading made use of graded density impactors called "pillows" [7] that produce a small shock upon direct impact with a sample, followed by a gradual increase in loading stress. Recently, this technique has been further advanced through computer-designed density impactors that improve flexibility in controlling the input pressure history [8]. However, the inescapable formation of the initial shock wave from the impact is undesirable for many experiments. Alternatively, an intense laser energy deposition technique has been developed that produces a stagnating plasma onto a planar specimen and shocklessly loads it to high pressures [9, 10], which is similar to the earlier high explosive technique involving the recompression of expanding detonation products [11]. The technique has been demonstrated to produce smooth compression with relatively short loading times of $\sim$ 10 ns. In addition, utilizing a laser whose intensity increased smoothly over $\sim$ 2.5 ns [12], a loading risetime similar to the laser pulse risetime has been generated with the ablative loading technique.

Magnetically driven isentropic compression using the Z accelerator has also been used to produce smooth continuous loading of materials to Mbar pressures. This was first accomplished in 1998 [13, 14] with a pulsed power technique involving the magnetic loading of thin metal plates. This scheme has proven to be quite successful, and has matured significantly over the last decade. At the Z accelerator [16], smoothly increasing compression of materials to pressures of several hundred GPa are now routinely used for quasi-isentropic loading EOS measurements [17, 18, 19, 20, 21], optical properties [22, 23], and phase transitions [24]. In this technique, planar load samples (6-10 mm in diameter by 0.5-1.5 mm thick) are mounted on a flat anode plate of either aluminum or copper. A direct short between the parallel anode and cathode plates allows a $\sim$ 20 MA, $\sim$ 100-300 ns risetime current pulse to flow from one plate to the other, which generates a planar time-varying magnetic field between the conductors. The resulting large magnetic pressure launches a high-pressure ramp wave into the anode conductor and hence into the planar sample. The advantages of this approach over the others discussed above are that a smooth, shockless compression is achieved, and loading time scales are similar to that of gas gun impact using graded density impactors [8]. At these comparatively lower compression strain rates of about 10^6 /s, dissipative contributions to material property measurements, such as equation of state and mechanical properties, are observed to be minimal in some materials such as aluminum [25].

Because the Z accelerator is a large experimental facility designed to accommodate multiple scientific programs needs, research using ICE loading to study material properties is hampered by limited available machine time, experimental constraints in fielding certain diagnostics, the large number of personnel needed to operate the machine, a long turn-around time, and considerable operational expense. Although the pulsed power technique has proven to be quite productive in the generation of ICE loading on the Z accelerator, several key issues need to be examined more thoroughly, such as the panel and sample preparation, the uniformity of loading, and the effect of edge waves on sample loading, for ICE experiments using a different pulsed power driver configuration.

To expand the use of pulsed power techniques for ICE studies a compact pulsed power generator, referred to as Veloce[1], was developed. Veloce was specifically designed for isentropic and shock compression experiments [26, 27, 28], and is both more accessible to experimenters and more economical to operate. The Z accelerator consists of Marx generators submerged in oil, water-dielectric pulse-forming lines, and magnetically insulated transmission lines in a vacuum, all of which occupy a large area of 30 m

[1]Veloce was constructed for Sandia National Laboratories by the companies of ITHPP (International Technologies for High Pulsed Power) and ITI (Ivanhoe Technologies Inc).

in diameter [16]. Other the other hand, Veloce is a low inductance generator based on a strip-line design first developed for the GEPI generator [29, 30], where no oil, water, or vacuum are used for insulation, thus making it much easier to operate and maintain. The GEPI machine produces a 3-4 MA, 600 ns current pulse, and its overall dimensions are L $\times$ W = 6 m $\times$ 6 m. Veloce occupies only a 3.6 m by 5.5 m area, and delivers up to 3 MA of current rapidly ($\sim$ 440-530 ns) into an inductive load where significant magnetic pressures are produced. The strip-line design has previously been used in the exploding of electrically heated metal foils [31]. In this case, the current pulse ($\sim$ 1 μs risetime) was used to explode thin Al foils ($\sim$ 0.05 mm thick) which generated large thermal pressures to accelerate thin flyer plates. On Veloce, the load electrodes are much thicker (1-2 mm) and the current risetime is faster, so the thermal pressure remains small compared to the magnetic pressure. The resulting magnetic pressure can be used either to drive ramp pressure waves (5-20 GPa) into material samples or to launch flyer plates (1-2 mm) to velocities of 1-3 km/s.

In this report, we briefly describe the basic concepts of isentropic loading and the experimental configuration used for the Veloce pulsed power generator. A discussion of the key experimental issues of panel and sample preparation, and uniformity of loading necessary to obtain accurate material studies, are presented. A description of the VISAR diagnostics fielded on Veloce is also presented. Finally, results of recent experiments on aluminum are also used to illustrate accuracy achievable with the method.

Chapter 2

Basic concepts of isentropic loading

Over numerous shock wave experiments, the high-pressure EOS of materials has been thoroughly described along the principal Hugoniot. Yet the Hugoniot represents only a single curve on the EOS phase space. Two other classes of curves of interest are the compression isotherms and isentropes. The isentropic curve generally lies in-between the isotherm and Hugoniot curves, is second order tangent to the Hugoniot at low pressures, and represents a reversible loading process. Whereas a shock experiment generally yields only the single final P-V point on the Hugoniot, an isentropic experiment yields a continuum of points along the isentropic loading path (see Fig. 2.1a). The actual loading curve is close to the path for isentropic loading in many cases, but not is precisely isentropic because of irreversible effects such as visco-plastic response and plastic work, and is referred to as quasi-isentropic.

The governing equations for planar shock loading of a solid initially at rest are summarized as [32, 33],

$$\sigma - \sigma_0 = \rho_0 U_S u_P, \tag{2.1}$$

$$\frac{V}{V_0} = 1 - \frac{u_P}{U_S}, \tag{2.2}$$

$$E - E_0 = \frac{1}{2}\left(\sigma + \sigma_0\right)\left(V - V_0\right). \tag{2.3}$$

In these equations, σ_0 is the initial longitudinal stress in the material, which is usually zero, σ is the longitudinal stress in the shocked state, ρ_0 is the initial mass density, V_0 and V are the initial and final specific volumes ($1/\rho$), respectively, E_0 and E are the initial and final specific internal energies, respectively, u_P is the material or particle velocity, and U_S is the shock velocity. Typically two variables such as shock velocity and particle velocity are measured in a steady shock wave experiment, allowing determination of the other three variables. Measurement of these variables produces a single point on the EOS surface. The locus of points produced by shock compression from the initial state to different final stresses is referred to as the principal Hugoniot for the material.

Similarly, the relations for isentropic loading of a solid initially at rest can be derived from the generalized conservation equations given as

$$\frac{\partial \sigma}{\partial h} = -\rho_0 \frac{\partial u_P}{\partial t}, \tag{2.4}$$

$$\frac{\partial V}{\partial t} = V_0 \frac{\partial u_P}{\partial h}, \tag{2.5}$$

$$\frac{\partial E}{\partial t} = -\sigma \frac{\partial V}{\partial t}, \tag{2.6}$$

where the derivatives are taken with respect to Lagrangian position h, and time t. In the Lagrangian reference frame, the coordinates are fixed to specific material or fluid elements which move in space. If the material response is strain-rate-independent, the motion becomes self-similar and the stress waves induced in the material are referred to as simple waves. For simple waves, the flow in an inviscid fluid, where longitudinal stress is equal to hydrostatic pressure, is isentropic ($S = S_0 = constant$) and Equations 2.4 - 2.6 reduce to:

$$d\sigma = \rho_0 C du_P, \tag{2.7}$$

$$dV = V_0 du_P / C, \tag{2.8}$$

$$dE = -\sigma \left(S_0\right) dV, \tag{2.9}$$

where $C = dh/dt$ is the Lagrangian wave velocity. Strictly speaking, isentropic flow is obtained only for an inviscid fluid, but the response for simple flow in solids is often used to approximate isentropic response [25]. The Lagrangian wave velocity is determined from the wave propagation properties of simple waves and is approximately related to the $U_S - u_p$ relation as,

$$C \approx C_0 + 2su_P, \tag{2.10}$$

where C_0 is the initial sound speed, and s is the parameter in the Hugoniot relation for shock speed [32],

$$U_S = C_0 + su_P. \tag{2.11}$$

Equation 2.10 may be obtained by differentiating Eq. 2.11, and should be a good approximation at low stresses (up to $\sim$ 30 GPa in Al) since the Hugoniot and Isentrope are similar .

In most materials, the local sound speed increases with increasing pressure as seen in the convex shape of the isentrope and Hugoniot in the P-V plane (see Fig. 2.1a). Continuous compression produces a ramp wave that will tend to steepen as it propagates into the sample (see Fig. 2.1c), and will eventually evolve into a shock wave, which has nearly discontinuous jumps in pressure, density, energy, temperature, and entropy (see Fig. 2.1d). Since wave evolution is governed by the local non-linear mechanical response of a material, measurement of wave evolution with propagation distance provides information on the continuous compression response at the corresponding loading strain rate [25, 34]. The standard method for obtaining EOS measurements along a compression isentrope involves the planar ramp loading of at least two samples of different thicknesses in which the thickness difference Δx is known precisely. The isentrope loading curve is reconstructed from the measured Lagrangian wave velocity histories of the rear surfaces of the samples (either free surface or window interface). It is important to note that for the Lagrangian analysis [34, 35], as long as the two sample 'EOS pairs' both experience the same pressure drive history, knowledge of actual input pressure wave profile is not required.

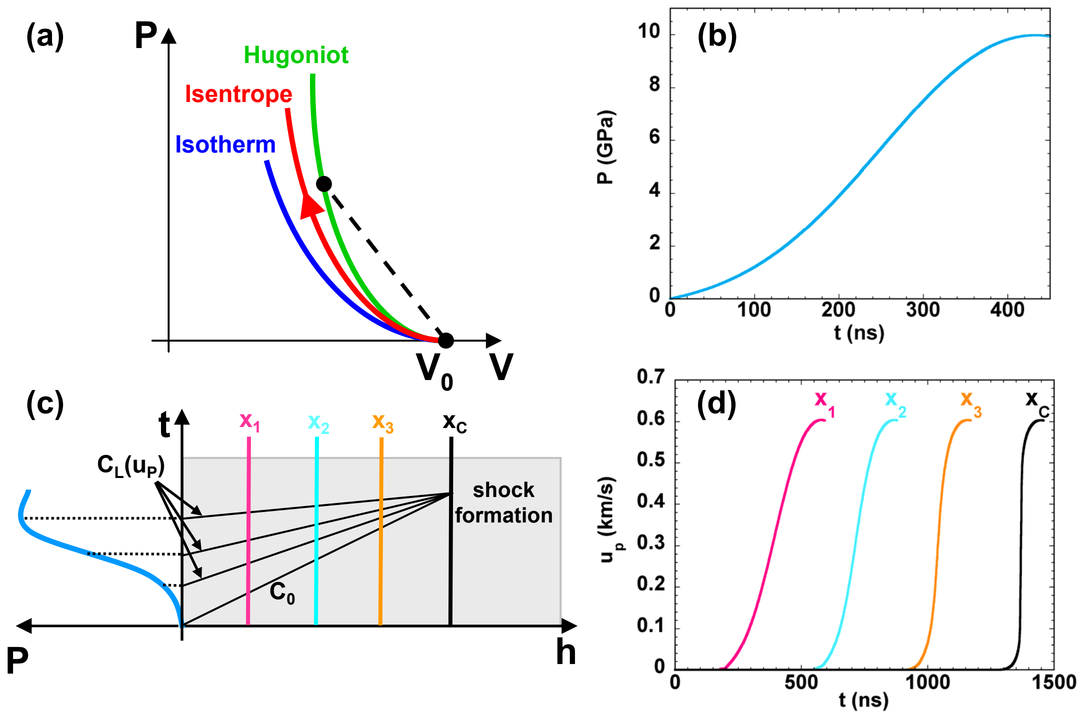

Figure 2.1. (a) Schematic of the isotherm, isentrope and Hugoniot curves for a material compressed to a high pressure state. (b) Typical pressure history applied to a sample for isentropic compression experiments, (c) propagation of the wave characteristics within the sample, and (d) particle velocities at various Lagrangian positions ($x_1 < x_2 < x_3 < x_C$) within the sample display the resulting ramp wave, and eventual shock wave formation at the "critical" location x_C.

Chapter 3

Experimental Configuration

3.1 Electrical layout and operation

An overhead view of the Veloce generator is shown in Fig. 3.1. The main electrical components consist of 8 main capacitors (Haefely-Trench, 3.95 μF each), 72 peaking capacitors (General Atomics, 0.1 μF each), a parallel plate transmission line (composed of 2 Al sheets, 2.5 m wide by 3.5 m long, separated by 20 layers of 0.1 mm thick Mylar), and a self-breaking "dynamic" switch assembly (DSA). The Veloce generator is basically a very powerful RLC peaking circuit as revealed in its equivalent electrical circuit (see Fig. 3.2). The electrical architecture and firing sequence of the machine is as follows. The 8 parallel main capacitors are charged (typically up to 70 kV) via a high voltage power source (Spellman SR6) with a charge time of approximately 60 s (charge current of $\sim$ 32 mA). A command fire is sent via a mini-Marx trigger generator to the coaxial switches of the main capacitors, causing them to discharge their stored energies (0.6 MJ) into the parallel plate transmission line. A voltage/current pulse, with a risetime of $\sim$ 700 ns, travels down the transmission line and charges the 72 parallel peaking capacitors. The peaking capacitors cause an oscillating response about the basic L_C ringing of the main capacitors, which boosts the peak current and shortens the current risetime to $\sim$ 600 ns. Next, the current pulse reaches the dynamic switch assembly, which encloses a load chamber containing the load region.

Inside the DSA, 64 self-breaking volume switch channels feed current into the load hex-plates of the load region where the load panels are connected to each other by a direct short. The current pulse risetime is controlled by adjusting the gas mixture of Ar and N2 gases which fill the DSA volume. With 100% Ar gas inside the DSA, the volume switches will break at $\sim$ 30 kV which results in a current pulse with a zero-to-peak risetime of 530 ns. By adding N2 gas to the mixture, the volume switches will have a higher breakdown voltage, thus shortening the pulse risetime. For a gas mixture of 20% Ar & 80% N_2, the volume switches break at $\sim$ 40 kV, and a shorter current risetime of 440 ns is achieved. The trade-off for the shorter risetime is a reduction in peak current reached. Because of the higher breakdown voltage of N_2, it was suspected that a few of the switch channels did not break, thereby reducing the current carrying capacity of the DSA. Additionally, it was supposed that the dynamic arc resistance was increased with the replacement of some Ar with N_2 [36].

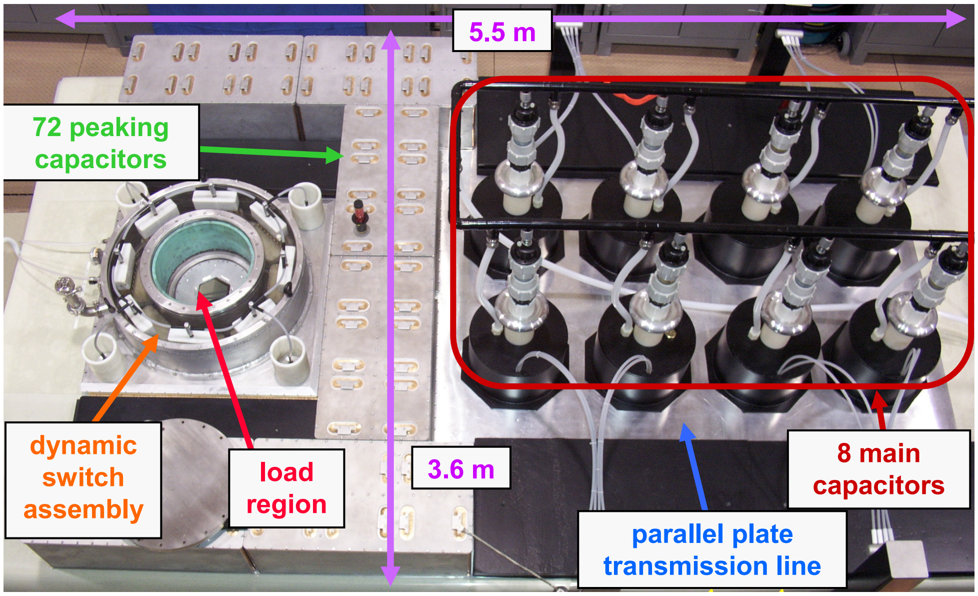

Figure 3.1. An overhead view of the Veloce pulsed power generator. Current flows, via the parallel plate transmission line, from the main capacitors to the peaking capacitors to the dynamic switch assembly, and into the load region.

Typical current profiles attained with the two limiting gas mixture setups are shown in Fig. 3.3a. As will be discussed in a later section, the resulting pressure pulse at the load is proportional to the square of the current pulse flowing into it, as shown Fig. 3.3b. Improvements in the pulse shaping on Veloce are still in development. The goal is to produce pulses with shorter risetimes (200-300 ns) and with more concave profiles, which will maximize ramp wave propagation distances before shock formation [20] and allow longer experimental recording times.

3.2 Load region

Figure 3.4 shows the arrangement for the load hex-plates and panels inside the load chamber. The hex-plates are circular Al plates (~ 30 cm diameter) with a hexagon cut out of the center area. At each side of the hexagon are machined grooves where load panels can be attached. For maximum current flow into the load panels, the "load location" on the hex-plates is situated nearest to the main capacitors. For each shot on Veloce, only one set of panels is utilized and thus destroyed. Additionally, some minimal damage occurs to the hex-plate at the load location. For the following shot, the hex-plates are simply rotated so that a fresh attachment groove is positioned at the load location. Typically, 5-6 shots can be performed on a set of hex-plates before they become too distorted in shape, due to the mechanical damage produced by the

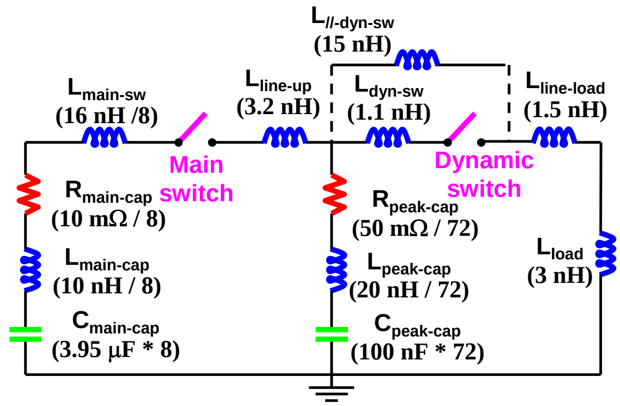

Figure 3.2. The equivalent electrical circuit of the Veloce pulsed power generator. $R_{main-cap}$, $L_{main-cap}$ and $C_{main-cap}$ are, respectively, the resistance, inductance and capacitance of the main capacitors. $L_{main-sw}$ is the inductance of the coaxial switches on the main capacitors, and $L_{line-up}$ is the inductance of the main line upstream of the peaking capacitors. $R_{peak-cap}$, $L_{peak-cap}$ and $C_{peak-cap}$ are, respectively, the resistance, inductance and capacitance of the peaking capacitors. L_{dyn-sw} is the inductance of the breakdown path of the dynamic switch, and $L_{\|-dyn-sw}$ is the inductance of the parallel path of the dynamic switch. $L_{line-load}$ is the inductance of the connection from the dynamic switch to the load, and L_{load} is the inductance of the load

large magnetic forces generated in the load region, and require replacement.

The efficiency of the Veloce generator has been examined in considerable detail. Although it was stated earlier that the Veloce pulser is able to generate up to 3 MA of current, the critical parameter is the amount of current that actually enters the load panels. Unfortunately, a direct measurement of the current within the load panels is rather challenging. Instead, it is more practical to measure, using a calibrated Rogowski coil surrounding the DSA, the total current entering the load region. In initial tests, Veloce was fired with a normal air environment in the load chamber. Typically in pulsed power generators, contaminants such as water molecules are removed by evacuating the load region to vacuum pressures of $\sim 10^{-4} - 10^{-5}$ Torr, whilst maintaining a high electrical breakdown voltage ($\sim$ 100 kV). However, because of the strip line design of Veloce involving sheets of Mylar and Kapton within the load region, a weak vacuum pressure of only $\sim 10^{-1}$ Torr was achievable in the load chamber. Unfortunately, this pressure corresponds to the bottom of the Paschen curve for electrical breakdown in air ($\sim$ 0.1 kV). When the machine was fired with this "vacuum" pressure in the load chamber, the Rogowski coil measured $\sim$ 20% increase in current entering the load region, yet the measured free surface velocities of the panels

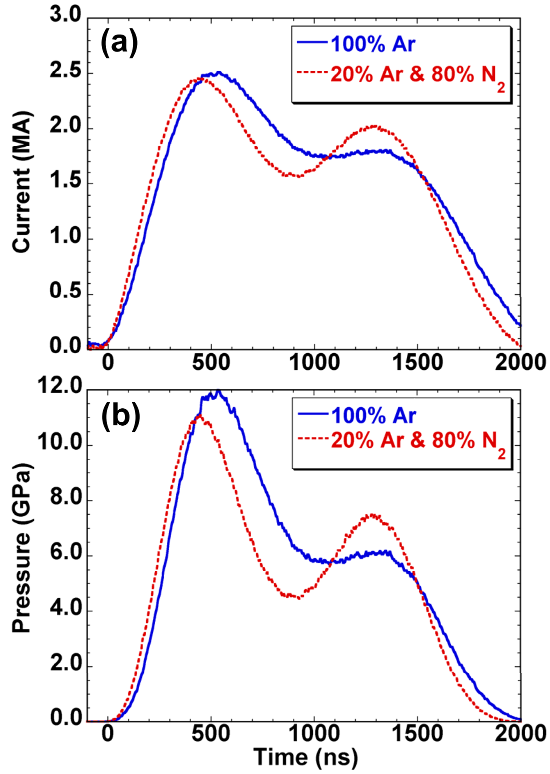

Figure 3.3. (a) Typical current profiles measured at the dynamic switch assembly for a 15 mm wide Al panel and (b) the resulting pressure pulses produced at the load.

decreased by $\sim$ 30%. Although more current entered the load region, less current actually went through the panels because of the electrical breakdown losses through the air. To resolve both contaminant and breakdown concerns, it was decided to first evacuate the load chamber to remove as much of the water molecules as possible, and then refill it with N_2 gas to normal atmosphere pressure ($\sim$ 1 atm) to regain a higher breakdown voltage. Using this procedure, Veloce operated optimally and provided the maximum current into the load panels.

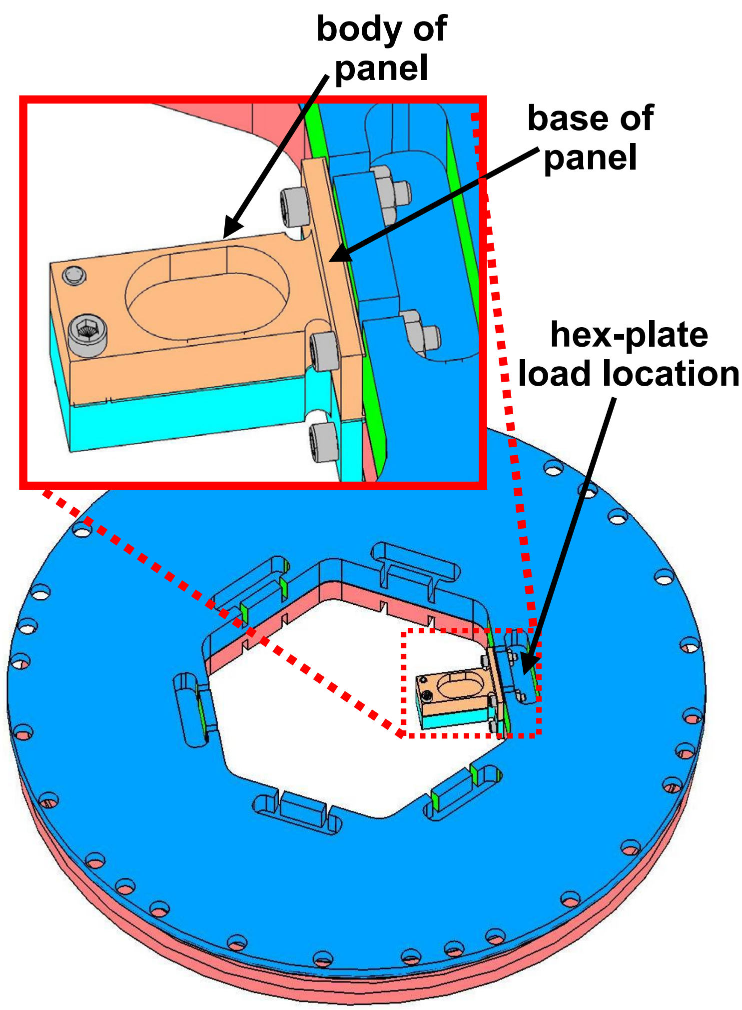

Figure 3.4. The assembled view of the top and bottom load panels attached to the top and bottom load hex-plates.

Chapter 4

Panel and sample preparation

4.1 Load panels

A cross-sectional view of the load region is shown in Fig. 4.1. Load panels are typically made from aluminum alloy 6061-T6, 1100 aluminum, or OFHC copper. Two load panels (designated as "top" and "bottom") are separated by 12 layers of Kapton polyimide film, each approximately 28 μm thick, which all together combine to a total thickness of 0.34 mm. The insulating Kapton constrains the current flow between the top and bottom panels to along the inner surfaces between them by means of a shorting current contact. Within the gap between the panels, strong magnetic fields are set-up perpendicular to the current path, and the resulting J $\times$ B Lorentz force produces magnetic pressures on the panels given as

$$P = k_E \frac{B^2}{2\mu} = k_E \frac{\mu}{2} \left(\frac{I}{w} \right)^2 . \tag{4.1}$$

The pressure P on the panels varies proportionately to the square of the current I divided by panel width w as given in Eq. 4.1, where k_E is an "experimental" coefficient, B is the magnetic field between the panels, and μ is the magnetic permeability between the panels ($\mu_{Kapton} \simeq \mu_0$, the magnetic permeability of free space). The magnetic pressure at the inner panel surface initiates a hydrodynamic wave that propagates through the load panels and reaches the outer panel surface where material samples are placed.

It is noted that the material properties of the load panels can influence the input stress history to the samples. The load panels have mainly been made from the aluminum alloy 6061-T6. For top and bottom panels with identical material properties, the drive histories will be the same, and their measured free surface velocities will be consistent with each other, as shown in Fig. 4.2a. Because of the large yield strength (Y_0 = 0.3 GPa) of Al 6061-T6, it was discovered that even a slight difference in the heat treatmet of the panels caused noticeable work hardening effects during loading. An example of top and bottom panels with slightly mismatched material properties is shown in Fig. 4.2b, a distinct divergence in the free surface velocities is observed near the elastic precursor. This would clearly introduce timing errors into the sample

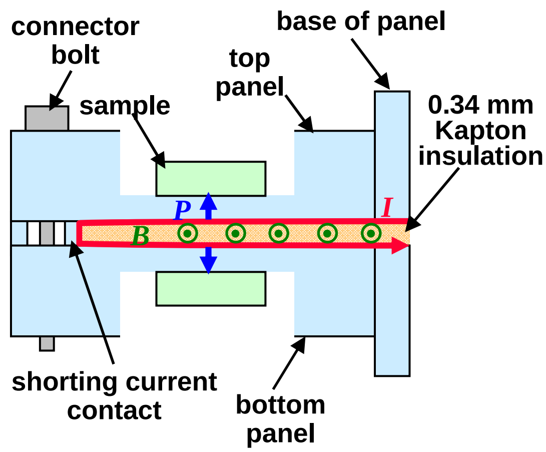

Figure 4.1. A cross-section view of the load region which depicts the J × B force exerted on the load panels and samples.

profiles near the elastic precursor. By reducing the thickness of the panels, and using materials that have low yield strengths such as aluminum 1100 or copper where difference in work hardening after elastic yeilding is small, any discrepancies in the material properties of the panels have been minimized. After resolving the material and timing issues, the input pressure histories to opposing samples agree to within 0.5 ns as shown in Fig 4.2c.

Looking from above, the overall shape of the panel consists of a long main body and a base of symmetric side supports (see Fig. 3.4). The "front" or current carrying sides of both panels are milled to a flatness of 5μm and then diamond machined to a surface roughness of $\sim$ 0.02 μm and flatness of 1-2 μm. Additionally, narrow current contacts extend out about 0.4 mm from the flat front surface of the bottom panel, as shown in Fig. 4.1. On the "back" side of the panel, a counter-bore is milled into the panel to allow the placement of load samples. The depth of the counter-bore into the panel depends on the experimental "drive" thickness requested. Selection of the panel thickness is based on two criteria; (1) shock formation, and 2) current front interaction. The first condition was briefly discussed in the previous section and places an upper bound on the panel thickness (see Fig. 1d). Because of the modest pressures attainable on Veloce (5-20 GPa), shock formation within the material does not occur until $\sim$ 5-6 mm in most materials, such as aluminum. Thus, the total panel and sample thickness is limited to $\sim$ 5 mm. The second condition is related to the reverberations between the panel/sample interface and the joule-heated current carrying region of the panel (see Fig. 4.3). Behind the pressure wave traveling within the panel is a current diffusion wave that ablates the front panel surface during the current pulse risetime. If the panel is too thin the ramp "foot" will reflect off the panel/sample interface and return to the joule-heated region prior to arrival of the

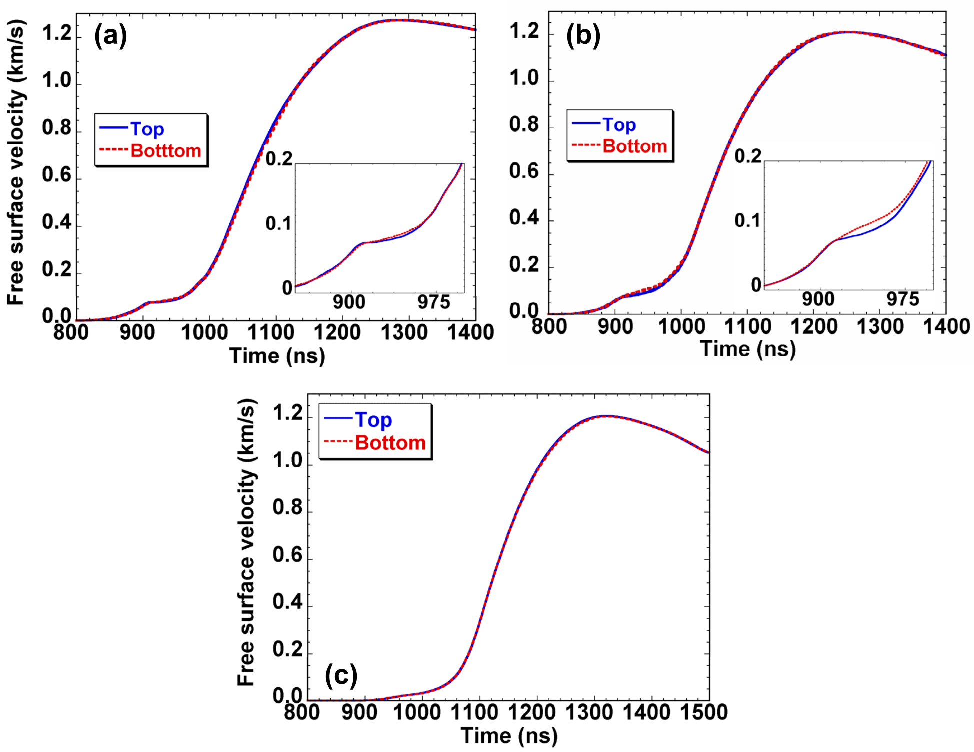

Figure 4.2. Measured free surface velocities of 2 mm thick by 15 mm wide by 35 mm long top and bottom Al 6061-T6 panels with (a) closely matched and (b) mismatched material properties; inset graph shows expanded view of elastic precursor. (c) Measured free surface velocities of 2 mm thick by 15 mm wide by 35 mm long top and bottom 1100 Al panels.

peak of the ramp, as shown in Fig. 4.3a. As this disturbance reflects off the density gradient at the diffusion front, it begins to bend the loading characteristics. Starting from the time this disturbance reaches the panel/sample interface, the data can no longer be analyzed using standard backward integration techniques [20]. By increasing the thickness of the panel, this wave reverberation phenomenon will be pushed later in time, and after the conclusion of the experiment, as shown in Fig. 4.3b. To meet both the described criteria panels are typically between 1.5-2 mm in thickness, and samples range in thickness from 1.0-3.5 mm. In addition, the rear side of the panel is diamond-turned to a finish of less than 20 nm. Some recent materials specimens studied on Veloce include aluminum (pure and various alloys), vanadium, tantalum, sapphire, lithium fluoride, and energetic materials. The typical sample sizes range between 10-17 mm in diameter. In order to obtain wave velocities with measurement errors of $\sim 1\%$, both the floor thickness of the panel and the sample thickness are measured precisely with a Nikon confocal NEXIV metrology system to $\pm$ 3 μm.

The other two key panel dimensions are the panel length and width. The initial panel

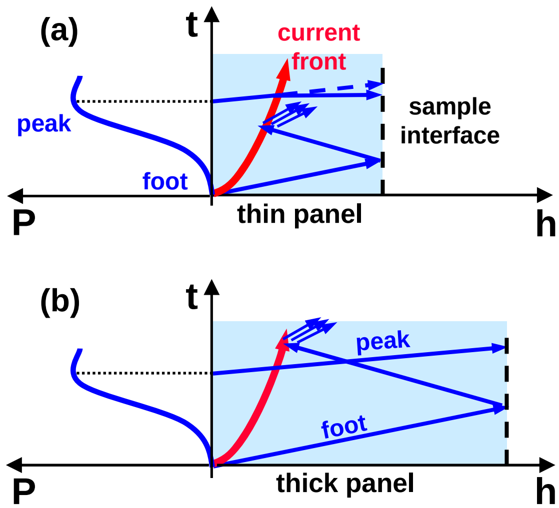

Figure 4.3. Sketch of the characteristic trajectories in the $t - h$ (time-Lagrangian position) plane, showing reverberation of the foot of the ramp wave between the panel/sample interface and the joule-heated material. (a) A thin panel where the reflection off the density gradient at the current diffusion front bends subsequent loading characteristics (i.e. from dashed line to solid line), invalidating backward analysis technique from that time forward. (b) A thick panel which avoids the wave reverberation.

design called for a panel length of 35 mm. This usually meant that on each panel only one sample could be placed on it in order to meet the requirements for 1-D loading of the sample. This will be discussed in a following section. To allow for the placement of a second sample, longer 50 mm panels were fabricated. Since there are two panels per shot (top and bottom), a total of 4 samples per shot can be studied on Veloce with this arrangement. However, a major drawback of lengthening the panels is that the load inductance of the panel is increased. Consequently, the total current into the panel is reduced, which in turn means a loss of magnetic pressure on the load. Alternatively, by narrowing the width of the panel the current density across the panel is increased, and thus the magnetic pressure on the load panel is increased as well. However, an obvious limit on how narrow the panel width may be is related to the lateral elastic and bulk release waves that travel initially with the ambient elastic longitudinal velocity but increase in velocity as the waves reaches higher stresses in the ramp wave, ultimately traveling at the elastic velocity at peak stress. These lateral waves emanating from the panel edge travel in spherical motion, which have wave velocity components normal to the longitudinal motion of the ramp wave and one along the longitudinal direction, which is increased by the particle velocity of the ramp wave at a given stress level. In addition, the lateral release waves must travel through longitudinal and lateral stress gradients in the panel. This is a very complicated problem, but can be approximated for designing ramp wave experiments by using the average elastic velocity to estimate arrival of lateral edge waves at the center of the sample where a recording VISAR probe is located.

Examples are presented in Fig. 4.4 to illustrate the effects of lateral release waves on measured longitudinal wave profiles for different size panels and for different panel materials. The examples consist of 10, 15, 20 mm wide panels made of either Al or Cu, each 2 mm thick. For this simple case, the panel itself is the sample, and the effects of lateral release waves from the edge of the panel were evaluated in the center of the panel. The drive pressure in each case was assumed to be uniform over the drive surface of the panel, MHD effects are neglected, and the recording point is assumed to be at the center of back surface of the panel, i.e., opposite the drive surface. A linear increase in drive pressure is assumed over a 450 ns interval with a peak of 10 GPa, and a fall of pressure to 60% of peak over an additional 300 ns. Using the approximate technique outlined above, the first arrival of lateral elastic release waves is estimated to occur at times of 0.74, 1.08, and 1.42 μs for the Al panels (Fig. 4.4a), respectively, and 1.01, 1.46, and 1.92 μs for the Cu panels (Fig. 4.4b), respectively. The arrival times for peak compression are 0.74 μs for aluminum and 0.87 μs for copper; the arrival times for unloading to the 60 % level are 1.07 μs for aluminum and 1.21 μs for copper, which include the full unloading profiles. First, it is noted that for the 10 mm wide, 2 mm thick Al panel, lateral elastic release waves arrive near peak compression, perturbing the complete unloading profile, whereas for wider aluminum panels the unloading profiles are unperturbed. Secondly, the perturbation times are delayed for the copper panels of comparable dimensions because of lower sound speeds. In this case, the unloading profile is perturbed for the 10 mm wide, 2 mm thick copper panel, but the full unloading profiles are unperturbed for the wider panels by a larger margin than for aluminum. Increasing the thickness of the panel requires a corresponding increase in width to maintain a relative unperturbed time. It is further noted that these calculations were performed for elastic lateral waves which are generally small in amplitude. Additional time is required for bulk lateral unloading waves to reach the recording surface because of their lower velocities. Although idealized for optimal loading/unloading and location of samples and diagnostics, these examples illustrate the importance of carefully designing the panels to mitigate the effects of lateral unloading over times of interest. Although the examples are for a single material, extension to two or more materials, which is more typical of actual Veloce sample configurations, is straightforward using the methodology outlined above.

4.2 Sample and window assembly

Usually, a laser-grade window is glued onto the back surface of the sample in order to observe the window/sample interface while the sample remains pressurized. The existence of "voids" between the sample and windows has routinely been an issue for the glue bonding of materials in ramp experiments. Suppose a void/gap exists in glue

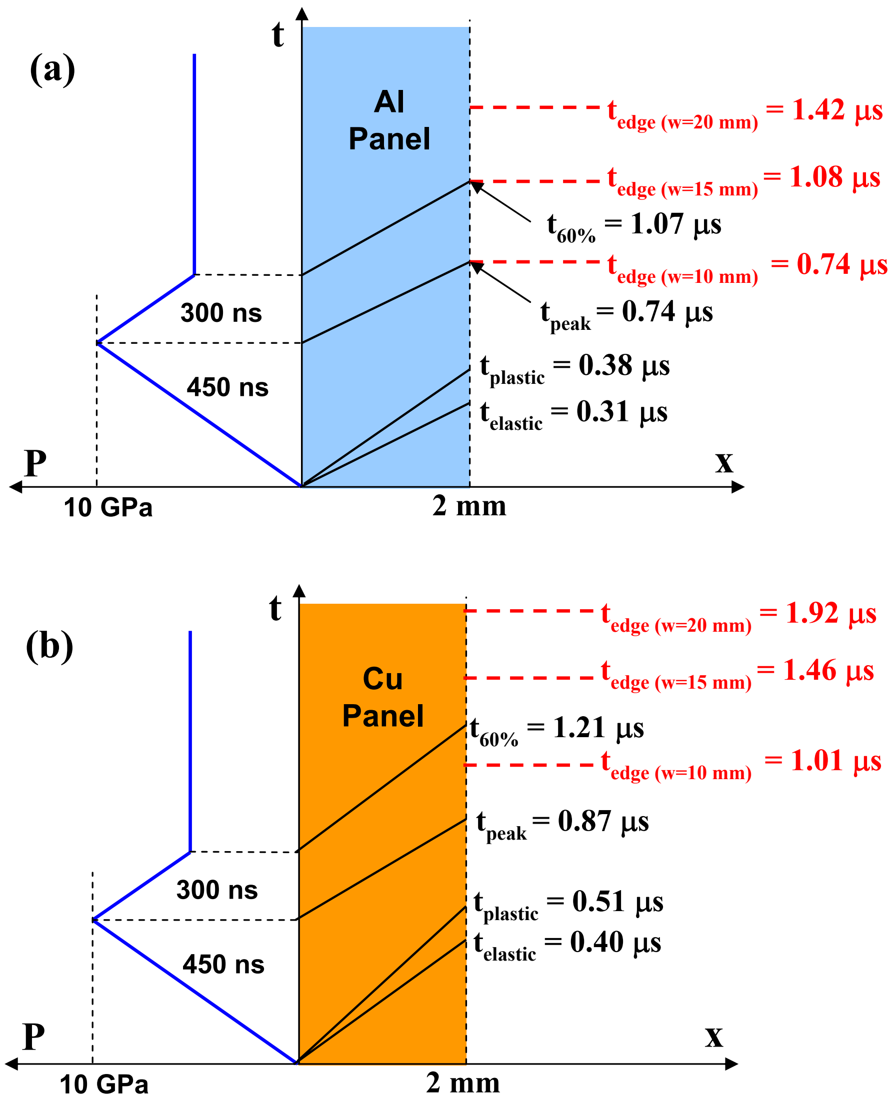

Figure 4.4. The x-t diagrams for (a) 2 mm thick Al panel, and (b) 2 mm thick Cu panel.

between the sample and window, and it has an area of ∼ a hundred μm in diameter, which is on the order of the spot size of a VISAR probe monitoring that location. As the ramp wave reaches the gap, the sample surface in the void region will be accelerated by the particle velocity at the foot of the ramp wave towards the window (see Fig. 4.5). For an increment in particle speed of ∼ 0.01 μm/ns at the ramp waves foot, a gap of 1 μm will take ∼ 50 ns to close during which time the window remains stationary. Once the gap is closed, impact of the sample against the window produces a noticeable shock jump of interface velocity. This "shock-up" disrupts the smooth continuous pressure loading profile desired for ICE work and produces a large error in measured transit time for the wave.

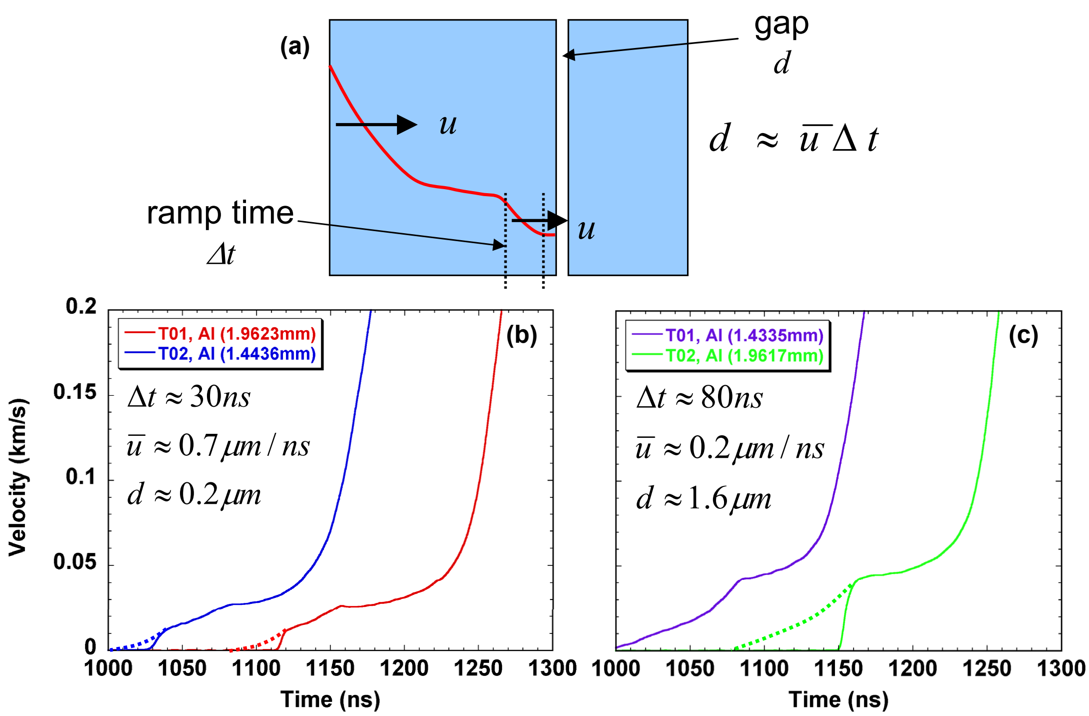

Figure 4.5. (a) Illustration of gap closure producing shock up with (b) a small gap of 0.2 μm, and (c) a large gap of 1.6 μm. The dashed lines represent the predicted unshocked ramp profiles.

The following procedure has proven to be successful in negating the gap closure problem. First, a small amount of ultra-low viscosity epoxy glue (Angstrom Bond) is mixed in a dish. The dish with the mixed glue is then placed in a vacuum chamber, which is evacuated for several minutes. During that time, any air pockets in the glue are bubbled out due to the lower pressure surrounding it. After removing from the vacuum chamber, a small amount of glue is applied to the center of a sample. Next, a window is set onto the sample, and the sample/window "load stack" is then placed under a continuous press apparatus. The load stack is kept under a constant pressure of 12-15 psi for 12 hours. Using this technique, typical glue layer thicknesses range between 0.5-3 μm with very low occurrences of gaps. A similar procedure is employed to glue the load stack to the rear side of the load panels. It is also noted the panel's rear side is now diamond machined with a slight convex height of ~ 1 μm, which also minimizes the formation of voids at the central location of the sample.

4.3 Load panel assembly

The load panels are assembled together in the load region in the following manner. First, the bottom panel, with its front surface facing down, is placed onto a flat granite slab. Next, the bottom hex-plate is placed on the granite slab such that a groove location aligns with the bottom panel for attachment. The bottom panel is attached to the hex-plate with bolts through the base of the panel (see Fig. 3.4). The bottom hex-plate and panel assembly is flipped over so that 6 layers (each ~ 28 μm in thickness) of Kapton can be laid upon it. To allow for the current contact between the top and bottom panels, a small area of Kapton near the current contact is cut and removed (see Fig. 4.6). From underneath the Veloce generator, this bottom assembly, with the Kapton layer overlaid, is bolted into the load region (see Fig. 4.7a). Next, 6 additional layers of Kapton, the top hex-plate are placed in the load region from above and aligned with the bottom assembly (see Fig. 4.7b). The top panel is then placed over the bottom panel and slotted into the top hex-plate groove location (see Fig. 4.7c).

The top and bottom panels are electrically linked by the "shorting" current contact, but are physically held together by a "connector bolt" (see Fig. 4.1). In the earlier load panel design, two current contact "feets" protruded from the current carrying surface of the bottom panel to provide the current short to the top panel. However, several disadvantages arose from this design. First, the added complexity of the current contact feets increases the cost and fabication time of the panels. Specifically, when diamond machining the current carrying for flatness, the diamond turning bit tool is unable to reach all the way to the current contact. As a result, near the current contact a small step (~ 0.5 mm wide) is created which is slightly elevated ($\sim 25\mu$m) above the rest of the panel. Furthermore, load panels with the smallest difference between their thicknesses ($\leq 5\mu$m) are usually matched together in order to obtain loading histories which are close to identical as possible. By having specific top and bottom panels, the number of matching sets of panels is more limited. In the more recent load panel design, the current contact feet are eliminated, so the top and bottom panels are identical with flat front surfaces along the entire panel lengths, and instead a separate current contact "shim" is placed in-between the top and bottom panels.

Originally, the base of the top panel was fastened to the top hex-plate with bolts as well. However, it was found that by fastening both the connector bolt at the

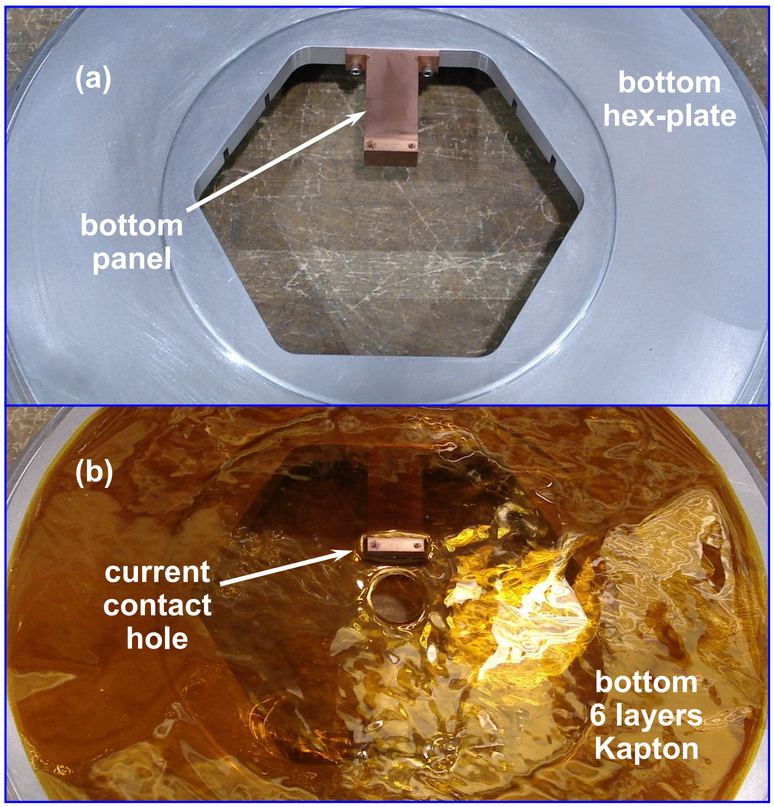

Figure 4.6. (a) Bottom panel connected to bottom hex-plate and (b) with bottom Kapton layers overlaid.

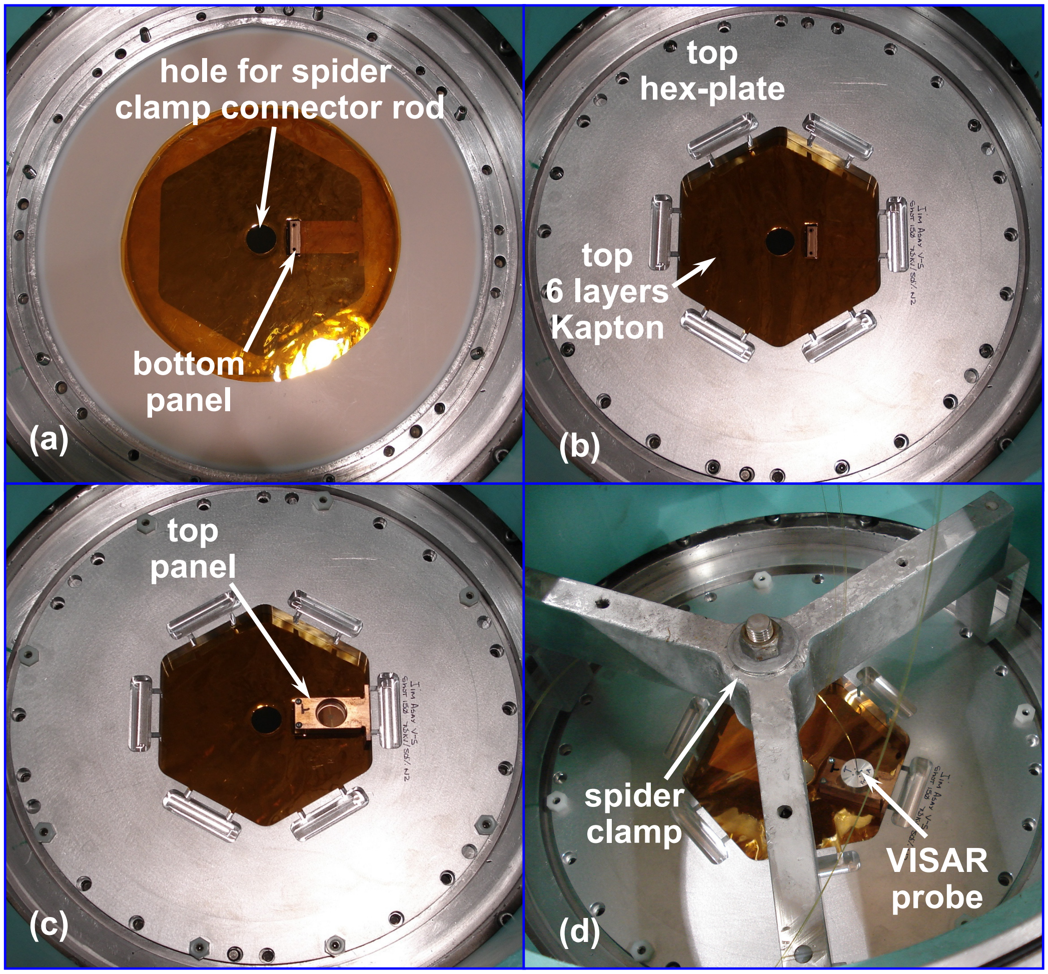

Figure 4.7. Load procedure as viewed from above Veloce.

current contact and the bolts at the panel base, stressing and warping of the top panel was likely to occur. In one incident, the sample glued to the top panel actually became dislodged during the fastening of the top panel. To avoid inducing stresses on the top panel, a thin aluminum foil ($\sim 40\mu$m) is first placed in-between the base of the top panel and top hex-plate. The top panel is then pushed up against the top hex-plate while only the connector bolt at the current contact is fastened, and thus creates a "floating" contact at the base of the top panel. Next, from above and below the machine "spider" clamps are placed into the load region (see Fig. 4.7d). A long connector rod, which passes through a hole in the Kapton layers and joins the top and bottom spider clamps, is tightened to restrict the top and bottom load region sections from seperating during the current flow. Finally, the panel caps holding the VISAR probes are glued to the back side of the panels. Afterwards, the top and bottom load chambers are mounted to the machine (see Fig. 4.8).

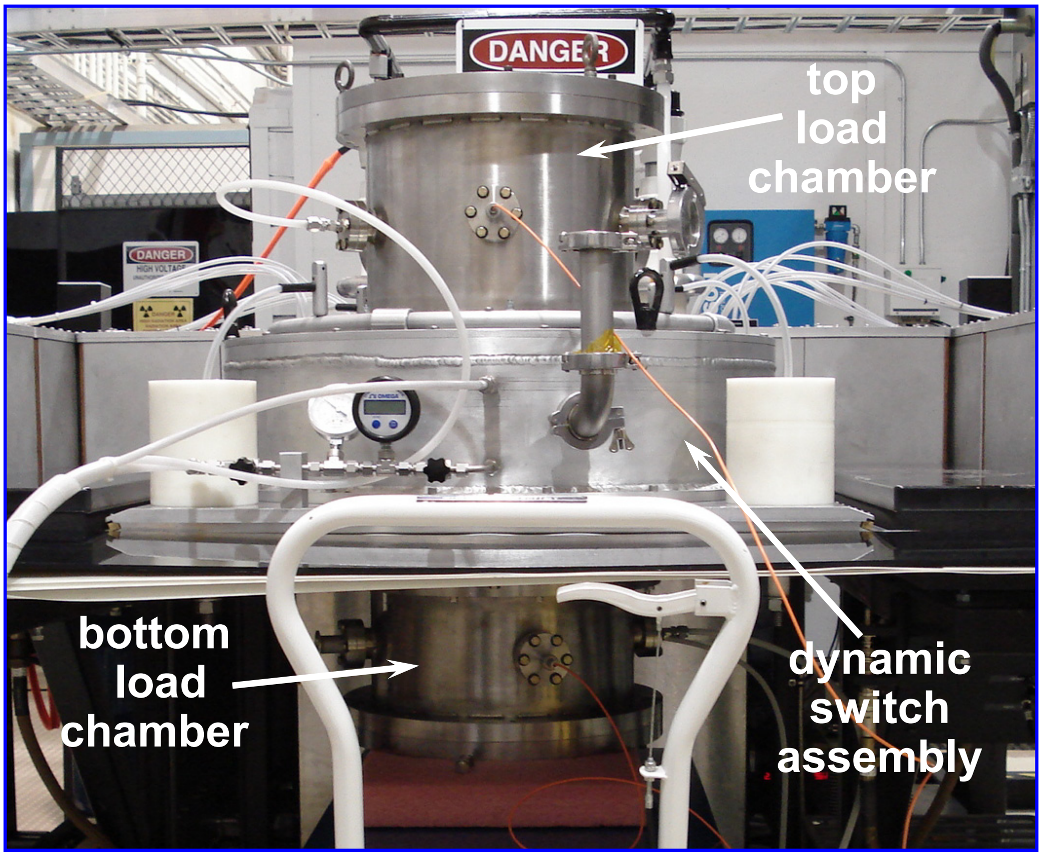

Figure 4.8. Front view of Veloce showing the top and bottom load chambers, and the dynamic switch assembly.

Chapter 5

Uniformity of Loading

The uniformity of ICE loading of planar samples has been studied extensively using both multi-point VISAR measurements and 3-D numerical simulations in preparation for application of the Veloce pulser to material studies. Fig. 5.1 shows the results of a preliminary experiment on 15 mm wide by 45 mm long Al panels. The free surface velocities were measured at three locations along the panel: (1) 11 mm, (2) 22 mm, and (3) 33 mm distance along the longitudinal axis from the base of the panel. A steady increase in the measured particle velocity from the lower panel section to the upper panel section was observed, as shown in Fig. 5.1b. Specifically, a velocity deviation of $\sim 5\%$ was observed between locations (1) & (2), and as much as 10between locations (1) & (3), as shown in Fig. 5.1c. An initial explanation for this on-axis nonuniform loading was that load panels were not completely parallel to each other. A description of an experiment to test the non-parallel panel hypothesis is given below. However, using numerical simulations it was shown that as current flows from the transmission line into the panel, complex nonuniformities in the current flow inherently develop on the current load surface of the panels. The results of the 3-D magnetohydrodynamic (MHD) simulations studying this problem are discussed in the following section. This is followed by a discussion of the effect that nonuniform loading has on experimental wave profile measurements.

5.1 Load panel parallelism

Based on the observed experimental observations of nonuniformity of the velocity measurements due to non-uniform current flow, it was hypothesized that instead of being perfectly parallel, the panels actually formed a wedge-shape with a smaller gap near the current contact and a larger gap at the base of the panel. However, the parallelism of the gap between the top and bottom panels in the load region is difficult to measure in the assembled configuration due to the layers of Kapton in-between the panels that prevent side access. Typically, the parallelism between the top and bottom panels is controlled by applying moderate downward force on the top panel as it is bolted to the bottom panel and the top hex-plate. However, it is possible that a slight wedge gap between the panels could be formed by the tightening of the connector bolt at the current contact and slight deviations of the bottom and

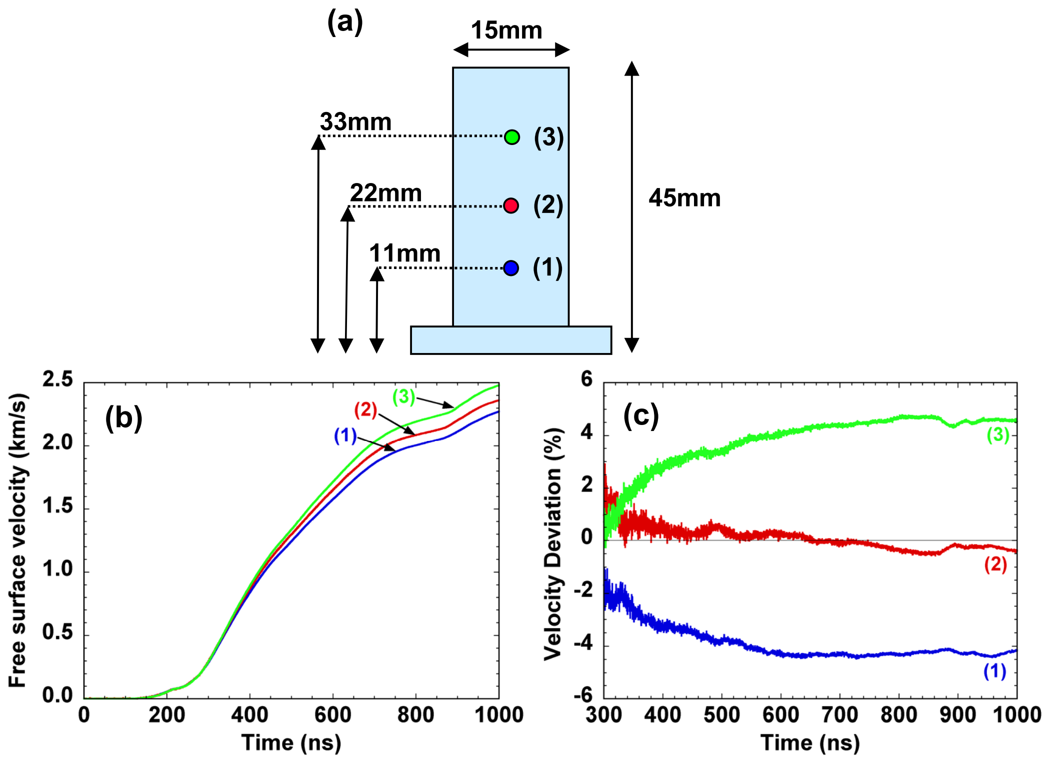

Figure 5.1. (a) A preliminary experiment showing the nonuniform loading of 1 mm thick by 15 mm wide by 45 mm long panels. (b) The free surface velocity measurements and (c) the percentage velocity deviation from the average velocity.

sides of the panel from a right angle.

Using a set of specially built screw clamps on the load panels, the effect of gap parallelism on measured velocity data was examined experimentally. The screw clamp consists of two narrow Al bars ($\sim 10 \times 10 \times 50$ mm), one placed over the top panel and the other under the bottom panel. The top and bottom bars are connected to each other via two long bolts near the ends of each bar. To measure the panel parallelism, the top and bottom panels are first assembled in the load region without any Kapton insulation between them. One screw clamp is then positioned near the current contact, while another is situated near the base of the panel. Gauge strips are then slid into the gap between the top and bottom panels to control panel parallelism. Finally, nuts on the bolts are tightened until the gap distance over the full panel length is set to 0.35 mm, at which point the positions of the nuts are marked off. Then, the clamps are taken off and the load panels disassembled. In addition to the usual hole for the current contacts, two additional holes for the bolts of the screw clamps are cut into the Kapton layers. The load panels are reassembled in the load region with the modified Kapton. The screw clamps are reattached to the panels and the nuts are set to the previously marked positions corresponding to the 0.35 mm gap distance. Finally, the panels are fastened to each other and the hex-plates, making sure not to perturb the set gap distance. With this “parallel assembly”, Veloce was fired and free surface velocities were measured along the panels. In the end, a comparison of the measured free surface velocities of the parallel assembly and the typical assembly showed no noticeable difference in peak particle velocity between them.

The results of the load panel parallelism test may be interpreted in two ways. First, in the typical assembly, the panels are as parallel as the panels in the carefully prepared parallel assembly. Alternatively, the panels in the typical assembly do form a slight wedge, but the small non-parallelism does not affect the loading of the panels. In either way, it was concluded that the typical assembly procedure for the panels was acceptable and it was not the cause of the nonuniformity in the pressure loading of the panels.

5.2 ALEGRA MHD modeling of panels

To further understand the cause of the non-uniformity of current distribution along the panels and to identify optimal sample locations on the panel that minimize gradients in the drive pressure for samples, 3-D simulations were performed with the ALEGRA code [37, 38, 39, 28]. ALEGRA is an arbitrary-Lagrangian-Eulerian (ALE) finite-element code that allows simulations of dynamic mechanical response and shock propagation in a resistive magneto-hydrodynamic (MHD) environment. The code includes hydrodynamics, solid mechanics, transient magnetics, thermal conduction, and radiation physics; and can be coupled to modern material models. The numerical simulations were conducted using a 3-D Cartesian, unstructured hexahedral Eulerian grid. To compare with measured particle velocity histories, the materials models employed in the simulations are also important. Equation of state models from the Sandia National Laboratories Sesame library [40] were used in the simulations. The material model for aluminum is described in reference [41], which includes densities ranging from 10^{-9} to 50 g/cm^3 for temperatures extending from 0 K to 10^5 K, and a classical elastic-plastic constitutive model for low stress response [42]. The aluminum parameters needed for the calculation are found in reference [43]. Finally, electrical and thermal conductivities were treated with the Lee-More-Desjarlais model, which includes the effects of magnetic fields [44, 45] and was found to be necessary for accurate simulations of magnetically accelerated aluminum flyer plates [39, 28]. The approach used was to first model the complete machine with coarse numerical resolution to determine the input current distribution to the hexagonal load region and load panels. The boundary conditions produced were then used to model the load panels with high resolution for comparison to experimental results.

5.2.1 Current angular distribution

In the Veloce pulser, the current flowing toward the load is not uniformly distributed around the hexagonal load region where the load is located. Due to the position of the main capacitors and the peaking capacitors, the current distribution will be higher on the hexagon side closest to the main capacitors, which is where the load panels are attached (Fig. 3.1). In order to estimate the current distribution, a simplistic version of the Veloce machine was modeled, from the main capacitors to the load, with the 3-D MHD ALEGRA code. The model did not include the peaking capacitors and the DSA because they were assumed to have a small impact on the current distribution, which is essentially determined by the load configuration at that location. Figure 5.2a displays the current density distribution in the hex-plate resulting from the simulation. Figure 5.2 shows the angular distribution of the current density expressed as the current fractional distribution at three radial positions on the hex-plate: r = 80, 110 and 142 mm. The current fraction at each angular location is calculated by dividing the current density at that angle ($\theta = 0 - 180°$) by the total current density within the circular area of radius r. The radial position $r = 142$ mm is located near the hex-plates outer edge, while the radial position $r = 80$ mm is closest to the hex-plates inner edge where the load panel is attached. Starting from the outer edge, the majority of the current flow is centered at the load panel location ($\theta = 0°$) and the rest comes from the remaining sections of the hex-plates. Since the load panel is a current-shorting path, as the current gets closer to the hex-plates inner edge it converges at the load panel. This current merging results in magnetic field bunching at the edges of the panel base, as will be shown in the following discussion.

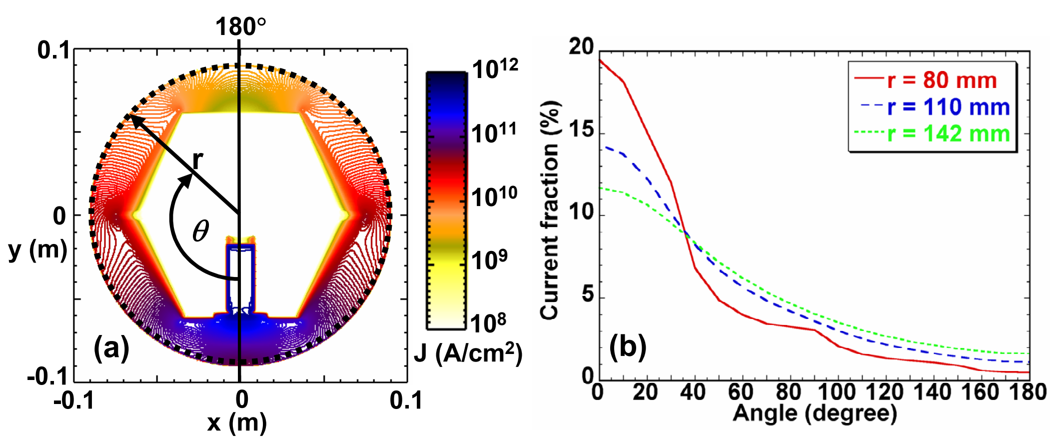

Figure 5.2. (a) The current density in the hex-plate and load panel; the coordinate system for the current distribution calculation with the load panel situated at $\theta = 0°$. (b) Angular distribution of the current density as a ratio of the total current density (for 10° wedges) at different radial positions r.

5.2.2 Load panel simulations

The 3-D MHD simulations, including the effects of cell resolution, were evaluated by comparing free-surface velocities measured in Veloce material experiments to those calculated with the ALEGRA code. An initial set of calculations included the load area as well as a portion of the hexagonal plates up to a radius of 9 cm, and were driven by the current measured at the Rogowski coil. The normalized current distribution around the perimeter of the simulation had a resolution of 0.94 mm (or 0.6°), and was determined by the calculation of the whole machine briefly described in the previous paragraph. These initial simulations were carried out with a numerical cell size of 0.4 mm along the width of the panel and 0.6 mm along the length of the panel. In the direction perpendicular to the panel, the numerical resolution had to be very fine because the panels are only 340 μm apart. A size of 42.5 μm for the numerical cells in the gap between the panels was chosen, which corresponds to 8 cells across the gap. However, the regions above and below the panels are only needed to allow the reconnection of the magnetic field and thus do not require high numerical resolution. Therefore, the mesh height was smoothly graded from 42.5 μm in the center of the gap between the panels to 1.0 mm above and below the top and bottom panels, respectively, to at the edge of the simulation area ($\sim$ 1.5 cm from the center). For these conditions, the calculated free surface velocity histories agreed with overall shape of the measured velocities, but the peak velocities only agreed within 3 to 5 %, depending on the position along the length of the panel. Also, for the size of the panel (15 $\times$ 35 mm), the resolution in the panel plane was only adequate for preliminary (exploratory) calculations and was too coarse to obtain accurate results, especially along the edges of the panel. In order to improve the resolution, the size of the simulation was reduced to just the panel and its base. The current distribution was determined by the previous calculations including a portion of the parallel plates. In this case, the current distribution used for boundary conditions was not normalized, but the driving current was scaled so that the calculated and measured free surface velocities would match. For these calculations, the size of the numerical cells was reduced to 0.25 mm in both directions of the panel. That resolution gave quantitatively equivalent values for the magnetic field but the results were smoother at the edges and corner of the panel. In the direction perpendicular to the panel, the 42.5 m resolution was retained between the two panels but it was smoothly graded to 0.75 mm, which corresponds to an expansion ratio of 1.05. The resolution of 42.5 μm used in the current flow region of the panel was somewhat coarse to precisely define the initial (cold) skin depth of about 69 μm at the beginning of the simulation. However, the current distribution in the plane of the current sheet was of most interest, which should be minimally affected by the resolution in the direction perpendicular to the current flow. Also, due to the high currents flowing in the panel near the peak value and the resultant heating of the aluminum, the current diffuses rapidly into the panel, which very quickly makes the 42.5 μm resolution adequate.

Figure 5.3 shows the comparison between ALEGRA calculations and Veloce measurements of the free surface velocities for a 2.5 mm thick by 15 mm wide by 35 mm long Al panel at three locations: (a) 13.5 mm, (b) 19.5 mm, and (c) 25.5 mm distance along the longitudinal axis measured from the base of the panel. This numerical resolution allowed an accurate calculation of the current flow, but resulted in calculated velocities at the foot of the pressure wave to deviate slightly from the measured velocities. Nonetheless, the overall shape of the calculated velocity profiles is consistent with the measurements, and the calculated peak velocities are in very good agreement with experiment. Furthermore, the relative changes in calculated velocity profiles at different positions on the panel show that the gradient in particle velocity and thus magnetic field is accurately modeled with the ALEGRA code.

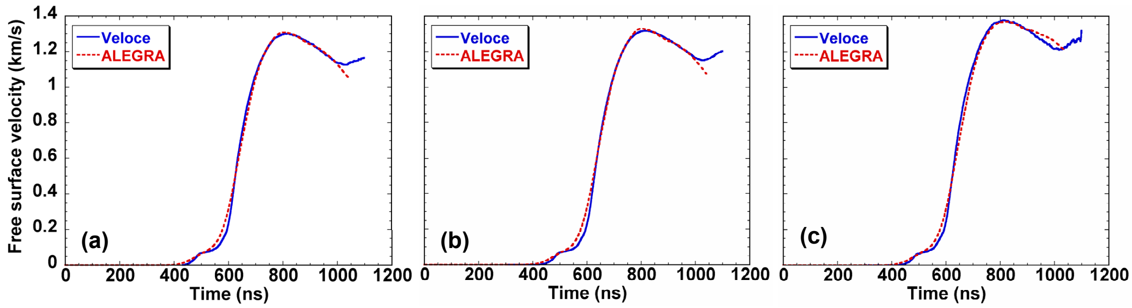

Figure 5.3. The comparison between ALEGRA calculations assuming hydrodynamic response and Veloce measurements of free surface velocities for a 2.5 mm thick by 15 mm wide by 35 mm long panel at (a) y = 13.5 mm, (b) 19.5 mm, and (c) 25.5 mm.

In the ideal case, the current flows uniformly and entirely on the inner surface of the panel, and so the experimental coefficient k_E of Eq. 4.1 is unity. In reality, the current also diffuses into the panel as time goes on, and is nonuniform at the panel edges, thus for the actual load panels $k_E < 1$. Distribution of the total input current measured by the Rogowski gauge on the panel drive surface and edges will depend on the specific panel configuration, material conductivity and time-dependent inductance of the load region. In general, the drive pressure on the panel will be lower than the theoretical response predicted by all of the input current evenly distributed on the drive surface. The experimental coefficient is the ratio of the effective current on the drive surface, as measured by the peak particle velocity to the theoretical prediction, which for 15 $\times$ 35 mm Al load panels was determined to be ~ 0.65. For experimenters without access to a 3-D MHD code, this information is valuable for estimating the loading pressure of prospective experiments. To avoid having to integrate the current density over the thickness of the panel, the magnetic field at the inner surface of the panel was used to describe the simulation results. Following Amperes law, the magnetic field at the inside surface of the panel is proportional to the current density at the same location, integrated over the thickness of the panel. The following summarizes the magnetic field distributions for a range of panel configurations and the resulting pressure gradients produced.

5.2.2.1 Reference panels

Fig. 5.4 displays the results of an ALEGRA simulation for the case of a 15 mm wide by 35 mm long Al panel. An image of the magnetic field at the inner surface of this reference panel is shown in Fig. 5.4a, which shows that the magnetic field is on the order of 100 tesla (1 megagauss). The panel length, or longitudinal axis, is plotted on the y-coordinate with the base of the panel situated at $y = 0$. The panel width is plotted on the x-coordinate and is symmetric about the center axis of the panel at $x = 0$. It is noted the current shorting contact, which connects the top and bottom panels, is located at $y = 30$ mm, above which there is negligible amount of current. The nonuniformities of the magnetic field on the panel are revealed in more detail by the contour plot shown in Fig. 5.4b. The contour lines represent changes of 0.5 T or about 0.5magnetic field. In addition to the enhanced magnetic field at the edges of the panels base, another magnetic field concentration is observed at the current contact. A typical 12 mm diameter load sample is overlaid on the panel, which provides insight into optimal location of the sample. By centering the sample at $y = 19.5$ mm, the minimal amount of nonuniformity in magnetic pressure is applied across the panel. Fig. 5.4c presents horizontal lineouts taken at the lower edge, middle, and upper edge of the sample ($y = 13.5$, 19.5, and 25.5 mm, respectively). At the lowest location, the magnetic field has a minimum at the center of the panel due to magnetic field concentration at the edges of the panel as the current enters it. This is apparent in Fig. 5.4c, which illustrates that the magnetic field is low at the panel center upon entrance of current to the panel. At the middle location, the magnetic field has nearly smoothed out across the panel, actually being slightly larger in the center of the panel. At the upper location, the magnetic field is seen to peak even more at the center of the panel, which is thought to be due to the current contact at the end of the panel. Nonetheless, at each location the horizontal nonuniformity is limited to only $\sim 0.5\%$ in magnetic field. From Equation 4.1, the pressure variation on the panel is related to the magnetic field variation by

$$\frac{\delta P}{P} \simeq 2\frac{\delta B}{B} - \left(\frac{\delta B}{B}\right)^2. \tag{5.1}$$

Thus, the pressure variation across the sample diameter in the lateral direction is constrained to $\sim 1\%$. On the other hand, a vertical lineout taken along the panels center axis reveals a more serious nonuniformity issue (see Fig. 5.4). First, as current flows from the hex-plate into the panel, the magnetic field increases rapidly from the initial level outside of the panel. The rapid increase occurs within the lower 8 mm of the panel, with a transition at this location to a more gradual increase. Moving further up the panel, the magnetic field steadily increases until the current contact is reached at 30 mm. Since negligible current exists beyond the current contact, the magnetic field is also rapidly extinguished. If the panels were infinitely long, then one would expect the magnetic field to be uniform with length. However, the shorting current contact adds an extra vertical component to the current, which produces an

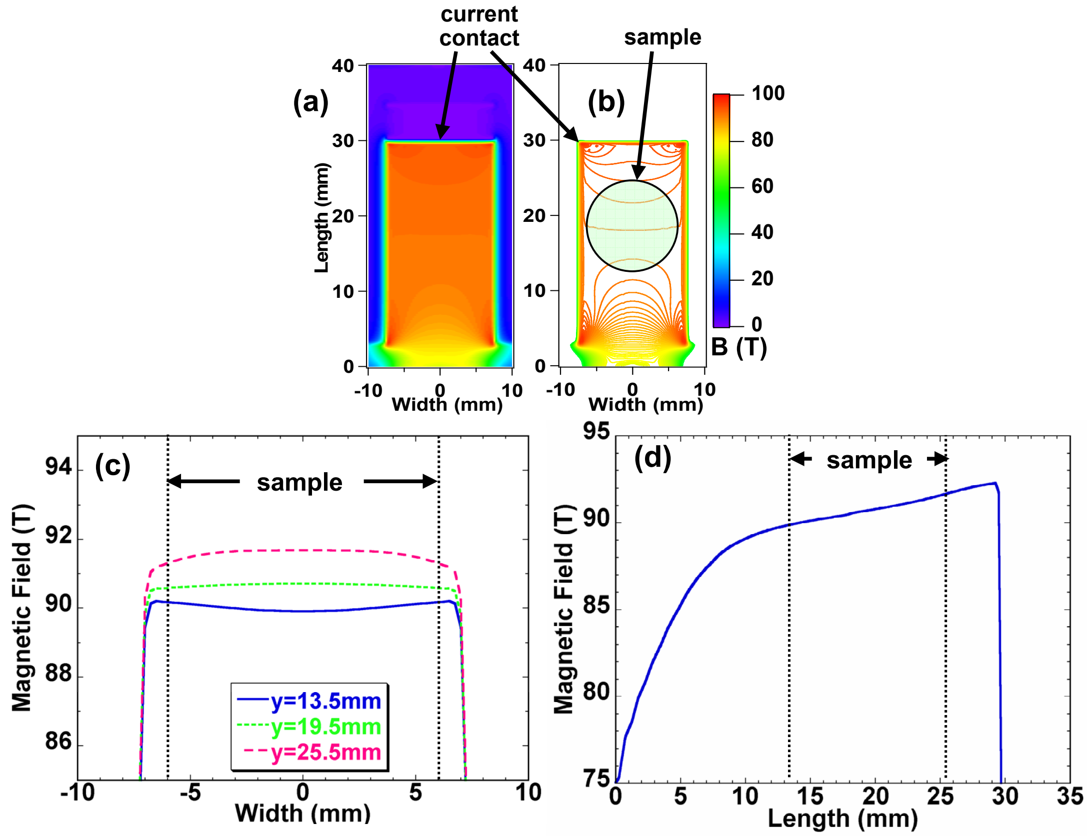

Figure 5.4. ALEGRA simulation of a 15mm wide × 35 mm long Al panel. The magnetic field at the inner surface of the panel; (a) an image, and (b) a contour plot; 0.5 T difference between the iso-field lines; with a 12 mm diameter sample placed at the optimal location. (c) Horizontal lineouts of the magnetic field at $y = 13.5$, 19.5, and 25.5 mm. (d) A lineout of the magnetic field along the panel's central axis ($x = 0$).

extra magnetic field contribution that varies as the inverse of the distance from the short. Hence the magnetic field close to the short is greater than the magnetic field close to the panel base. Even with the optimal sample placement at $y = 19.5$ mm, an approximately 2% variation in magnetic field or a little over 4% in pressure exists between the samples lower and top edges.

5.2.2.2 Long panels

To minimize nonuniformities in pressure drive and thus maximize the experimental accuracies possible with Veloce, a multiple-sample panel design was studied. By lengthening the panel, an additional sample may be placed on the back surface, while achieving better uniformity of loading. Fig. 5.5 displays a comparison between the reference panel (15 × 35 mm) with a modified long panel (15 × 50 mm). As shown in Fig. 5.5c, the central axis magnetic field vertical lineouts of the two panels are similar in shape. The overall magnetic field intensity on the long panel compared to the reference panel is reduced by ∼ 7%, or a pressure loss of ∼ 14%. However, a longitudinal variation in magnetic field of about 1% for a single sample or 1.3% for two samples is an improvement over the 2% variation observed for the reference panel sample (see Fig. 5.5d).

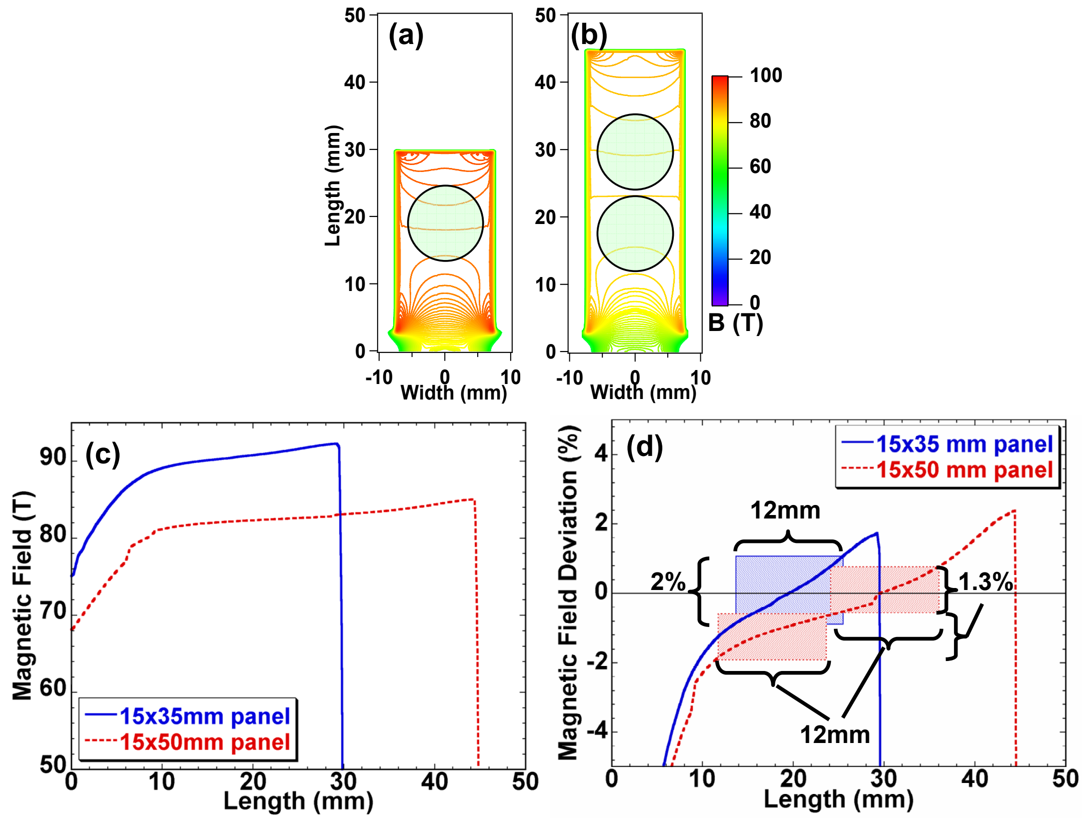

Figure 5.5. The magnetic field contour plots at the inner surface of (a) a 15 × 35 mm panel with a 12 mm diameter sample placed at the optimal location, and (b) a 15 × 50 mm panel with two 12 mm diameter samples placed at the optimal locations; 0.5 T difference between iso-field lines. (c) The magnetic field, and (d) the magnetic field deviations at the central axis of the two panels.

5.2.2.3 Wide panels

To accommodate larger load samples (up to 17 mm in diameter), a wide panel design was evaluated. Fig. 5.6 depicts a comparison between the reference panel (15×35 mm) with a wide panel (20×45 mm). As shown in Fig. 5.6c, there is a noticeable difference in the longitudinal profiles of the central axis magnetic field vertical lineouts of the two panels. In the reference panel case, the magnetic field in the hex-plate region was lower than at the entrance to the panel. On the other hand in the wide panel case, the magnetic field is actually lower on the panel than on the hex-plate region; thus there is an initial rapid drop in magnetic field at the panel base. Additionally, due to the spreading out of the magnetic field, there is a significant decrease of $\sim 33\%$ in the overall magnetic field, or about 55% in pressure, on the wide panel compared to the reference panel. Since the wide panel is also slightly longer than the reference panel, the magnetic field variation along a 17 mm sample diameter is only 1.7% (see Fig. 5.6d).

5.2.2.4 Notched panels

The introduction of "current shaping notches" near the base of the panel was suggested as a way to diminish the nonuniformity of current on the panels[1].The notch serves to force current toward the center upon entrance to the panel. To critically evaluate this effect, semi-circular notches were studied both experimentally and with numerical simulations. Although a systematic study of this effect had not been previously conducted, the present experiments showed a noticeable effect in current uniformity along the central longitudinal axis of the panel as the notch size was varied. To quantify this effect in more detail, the ALEGRA code was used with 3-D MHD capabilities to elucidate the effect of notch size on panel nonuniformity. In the simulations, semi-circular notches with varying radii were cut into both sides of the panel body near the panel base.

The magnetic field contour plots for panels with different notches sizes (0, 0.5, 1.0, and 1.6 mm in radius) are shown in Fig. 5.7. The 0 mm diameter notch case (Fig. 5.7a) represents the reference panel configuration. The notches are observed to effectively direct the magnetic field concentrations at the panel edges towards the panels center region. It is found that the larger notches produce a larger concentration of field near the panel entrance, but also produce considerably more distortion of the field lines in this region. Fig. 5.7e illustrates the longitudinal lineout distributions of magnetic field taken along the panels central axis for the different notch sizes. Obviously, when the notches are relatively large, there will be over compensation of the current focusing, as shown in the case of the 1.6 mm notches. In addition, the magnetic field variation in the upper section of the panel is not significantly affected by the notches, as shown in the Fig. 5.7f. Experimental tests on 15 x 35 mm panels with 1.0 and 1.5 mm notches

[1]G. Avrillaud, ITHPP, private communications, 2006

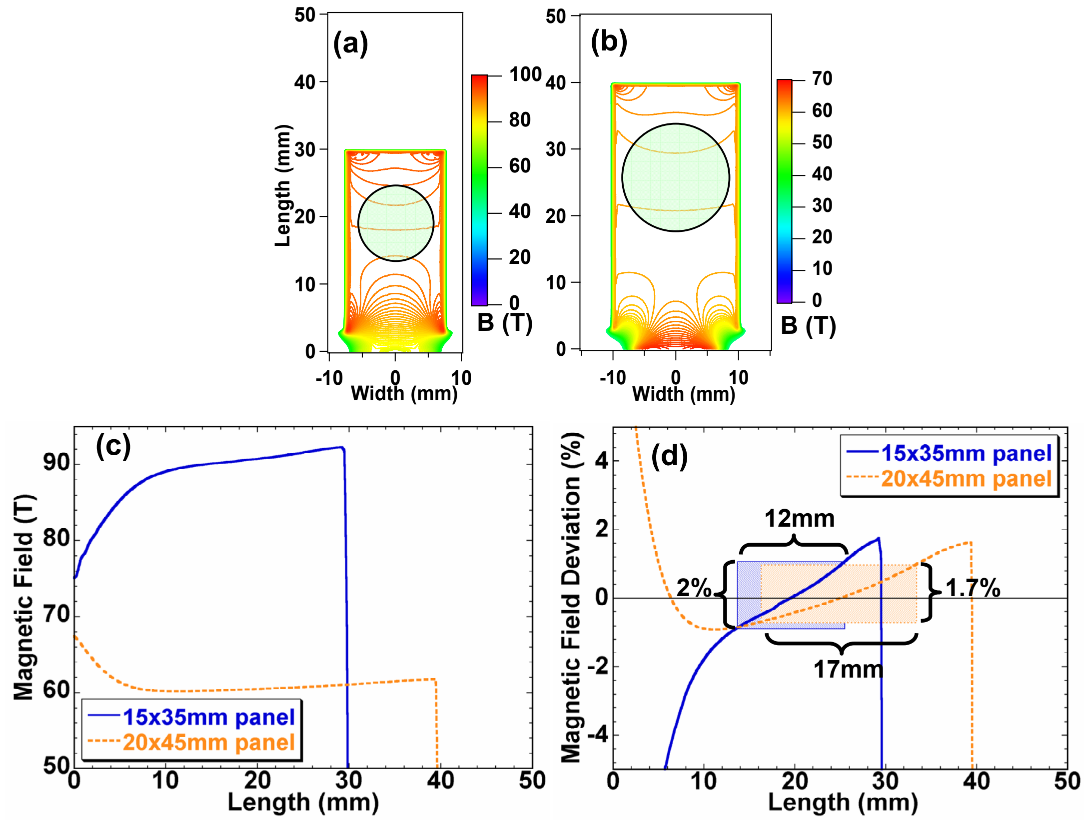

Figure 5.6. The magnetic field contour plots at the inner surface of (a) a 15 × 35 mm panel with a 12 mm diameter sample placed at the optimal location, and (b) a 20 × 45 mm panel with a 17 mm diameter sample placed at the optimal location; 0.5 T difference between iso-field lines. (c) The magnetic field, and (d) the magnetic field deviations at the central axes of the two panels.

have reproduced these pressure variation effects. Based on the results, notches of 1.2 mm in radius have been implemented on all load panels.

5.2.2.5 Tapered panels

Since the magnetic field produced at the panel surface is proportional to current density, or I/w, as shown in Eq. (14), it was thought that an alternative design to reduce the panel nonuniformity would be to taper the width of the panel from the entrance end to the shorting end. As discussed in the previous sections, the magnetic field intensifies from the input end of the panel to the upper part of the panel. Widening the panel linearly along its length should thus counteract the increasing

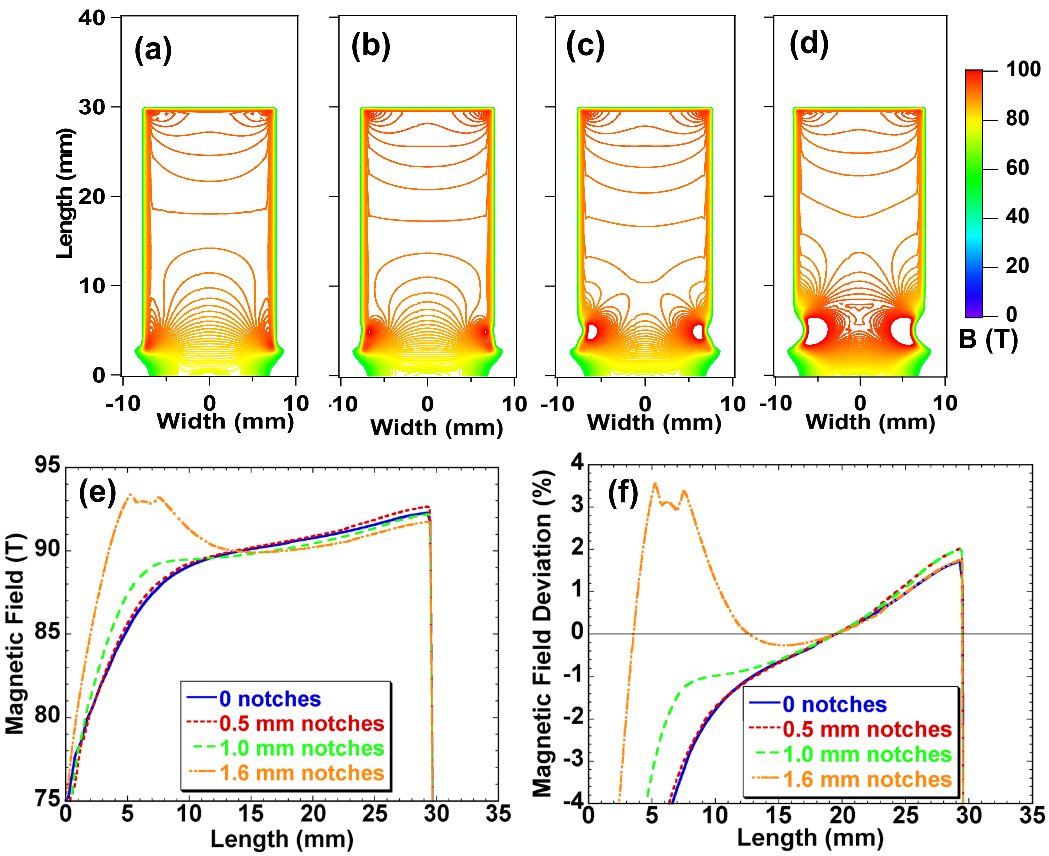

Figure 5.7. The magnetic field contour plot at the inner surface of a 15 mm wide by 35 mm long panel, with notches of radius (a) 0 (b) 0.5 mm, (c) 1.0 mm, and (d) 1.6 mm; 0.5 T difference between iso-fieldlines. Lineouts along the central axis of the panel; (e) the magnetic field, and (f) magnetic field deviation from the sample midpoint (y = 19.5 mm)

effect of field in the straight panels by decreasing the field linearly along the length. From the panel base to the panel upper edge, the panel width was increased linearly from the initial width $w = 15$ mm to $(1 + n\%)w$. Fig. 5.8 shows the magnetic field contour plots for panels with different width-tapering ($n = 0\%, 5\%, 7.5\%$, and 10%). The 0% taper case (Fig. 5.8a) corresponds to the reference panel. Fig. 5.8e shows the vertical lineouts of magnetic field taken along the panels central axis for the different taper cases. The benefits of the tapering in reducing nonuniformity are not evident until the width increase of the panel is greater than 5%. With a taper of 7.5%, the magnetic field variation within the diameter of a sample is diminished to $\sim 0.5\%$ (see Fig. 5.8f) or a pressure variation of $\sim 1\%$. This is achieved at a cost of a 5% decrease in overall magnetic field or 10% drop in overall pressure. Furthermore, over-tapering of the panel is seen in the case of the 10% taper, where the magnetic field at the current contact is less than the level in the lower section of the panel. Based on the results, if the pressure reduction is acceptable then the tapered panel design is a good way to improve drive pressure uniformity. Since it is of interest to maintain as much pressure as possible, the following panel design was also investigated.

5.2.2.6 Modified current contact panels

Lastly, the effect that the current contact has on the magnetic field variation on the panel was examined. As described in the earlier section, the magnetic field is established between the panels by the current path flowing along the inner surfaces of the panels, as shown in Fig. 4.1. An expanded view of the way the magnetic field lines wrap around the panels is illustrated in Fig. 5.9a. The current path on the bottom panel directed toward the end of the panels is straight until it makes a 180° hairpin turn at the current contact. This results in the bunching of the magnetic field lines at the edges of the current contact, which in turn increases the magnetic field near the end. To remedy the magnetic field hot spots, the panel widths were widened directly at the shorting contact, producing a set of "ear", as shown in Fig. 5.9b. The current contact ears extend the path that magnetic field lines must follow in wrapping around the panel, thus dispersing the magnetic field at the edges. Fig. 5.10 shows the comparison between the magnetic field near the current contact for the reference panel and the modified current contact panel. The panel ears are shown to effectively smooth out the magnetic field concentrations near the current contact (see Fig. 5.10b).

5.3 Pressure variation along panels

As in the previous discussion, the pressure variation in loading across the drive surface of the samples can be on the order of $\sim 2-4\%$ if the improvements in uniformity discussed above are not implemented. The major variation in pressure appears to occur along the longitudinal axis, with the lateral variation typically less than 1%

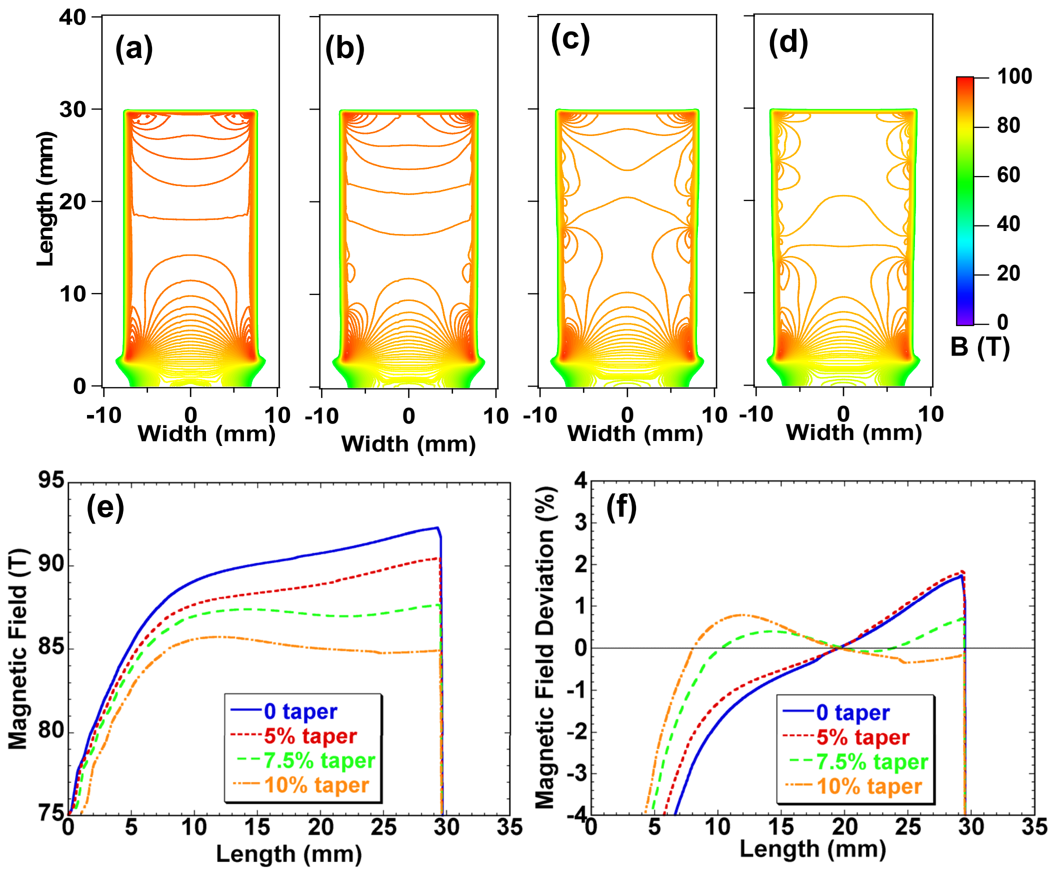

Figure 5.8. The magnetic field contour plot at the inner surface of a 15 mm wide by 35 mm long panel, with panel tapering of (a) 0 (b) 5%, (c) 7.5%, and (d) 10%; 0.5 T difference between iso-field lines. Lineouts along the central axis of the panel; (e) the magnetic field, and (f) magnetic field deviation from the sample midpoint (y = 19.5 mm).

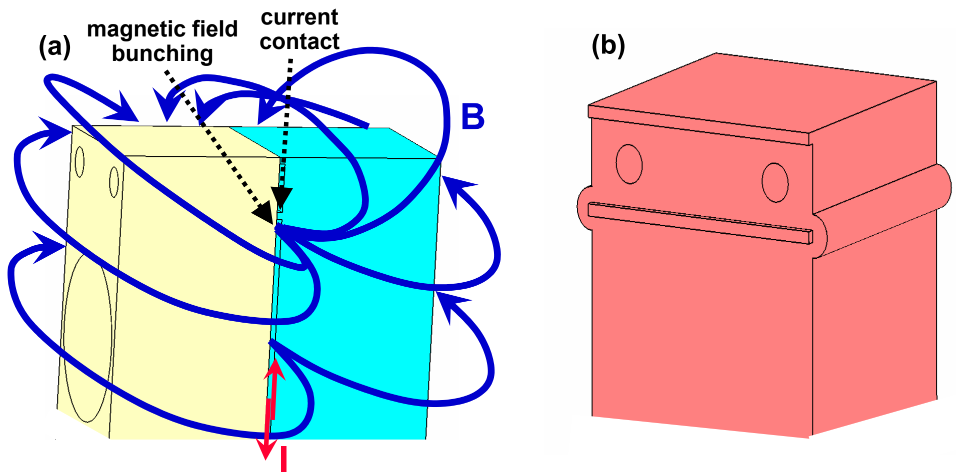

Figure 5.9. (a) An illustration of the magnetic field bunching at the current contact. (b) A modified current contact panel with "ears" extending out at the current contact to disperse the magnetic field lines.

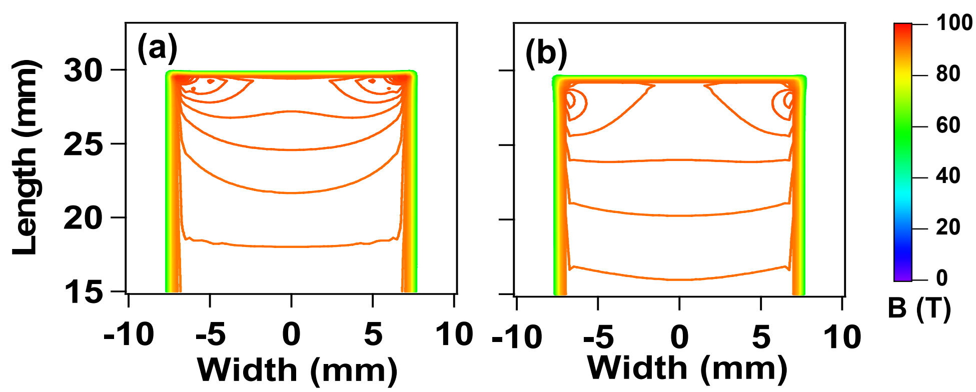

Figure 5.10. The magnetic field contour plots of (a) the 15 × 35 mm reference panel, and (b) the 15 × 35 mm modified current contact panel with "ear" 1 mm in radius; 0.5 T difference between iso-field lines.

out to the outer periphery of the sample. Two-dimensional simulations are therefore a good approximation for modeling the input pressure variation because of the predominant nonuniformity along the panel axis. To address whether longitudinal variations of up to 4% in drive pressure produce significant errors in EOS measurements, 2-D planar simulations were performed using the CTH hydrocode [46]. CTH is a multi-dimensional Eulerian shock-physics code that incorporates a variety of material models in numerical simulations. In the present application, an elastic-perfectly plastic material model was used to model an aluminum sample of 10 mm width to simulate the actual sample dimensions used in an experiment. To resolve the stress wave history, cells of 20 μm in size were used, and reflective boundary conditions were applied at the outer width of the sample.

In the calculations, a time-varying ramp wave loading was incorporated, using a spatial series of energy sources to deposit energy in a thin gas layer over a 10 mm wide panel front surface [47]. This simplified method reproduces a time-varying magnetic pressure loading at the drive surface without the detailed analysis of the MHD fields and is thus an expedient for simulating the actual pressure histories used in Veloce experiments. The gradient in load pressure along the input surface was varied from 0-4% by continuously varying the gas pressure from one edge of the sample to the other, as illustrated in Fig. 5.11a. This spatially and temporally varying pressure profile $P(x,t)$ was applied to one side of the Al sample using a Mie-Grneisen EOS for aluminum ($C_0 = 5.24$ km/s, $s = 1.40$, $Y = 0.42$ GPa, $\nu = 0.34$). Lagrangian tracers were monitored at the Al input surface to assure that a linear variation of the stress state was correctly imposed. Additional tracers were incorporated at 1 mm and 2 mm into the sample and tracked to determine the downstream stress histories produced by the imposed input profile. Three sets of calculations were performed using pressure profiles with linear pressure variations of 0%, 2% and 4% across the samples, which span the measured longitudinal variations on the panel, as discussed earlier. From the earlier discussion of lateral effects, the loading profiles are not influenced from lateral elastic perturbations, but the unloading profiles are affected.

The numerical simulations illustrate the effects of a combined linear input pressure gradient and 2-D wave propagation effects. The calculated wave profiles at 1 and 2 mm in the sample were used as "experimental data" and analyzed with a Lagrangian analysis technique. The wave profiles and resulting Lagrangian wave velocities for the three cases are presented in Fig. 5.11b and 5.11c, respectively. The resulting EOS and strength properties estimated for the three cases are summarized in Table 5.1. Since the 2-D wave interactions were a function of longitudinal direction, this effect produced slight errors in the calculated Lagrangian properties, such as wave velocities, particularly for unloading. Although these gradients produced less than 1% errors in stress and strain for loading, up to $\sim 2\%$ errors in stress and strain were observed during unloading. Since estimates of strength properties were derived from the difference between loading and unloading, errors in strength of $\sim 3\%$ and $\sim 5\%$ were obtained for 2% and 4% gradients when compared to the 0% gradient case (Fig. 5.11d). Error analysis of the Lagrangian analysis of multiple wave profiles, which arise from statistical errors due to uncertainties in the measured wave and particle velocities, leads to the error in estimating strength to be on order of 8% [48]. Since the errors due to the pressure nonuniformities are comparable to the statistical errors, every effort should be made to reduce spatial gradients in the drive pressure when using this magnetic loading technique, especially for unloading wave measurements.

Table 5.1. Input EOS and strength values used the 2-D simulations, and the output estimates of the EOS and strength.

	Pressure Variation	C_0 (km/s)	s	Y (GPa)
Input	-	5.24	1.400	0.420
Output	0%	5.25	1.401	0.402
	2%	5.25	1.405	0.390
	4%	5.23	1.410	0.381

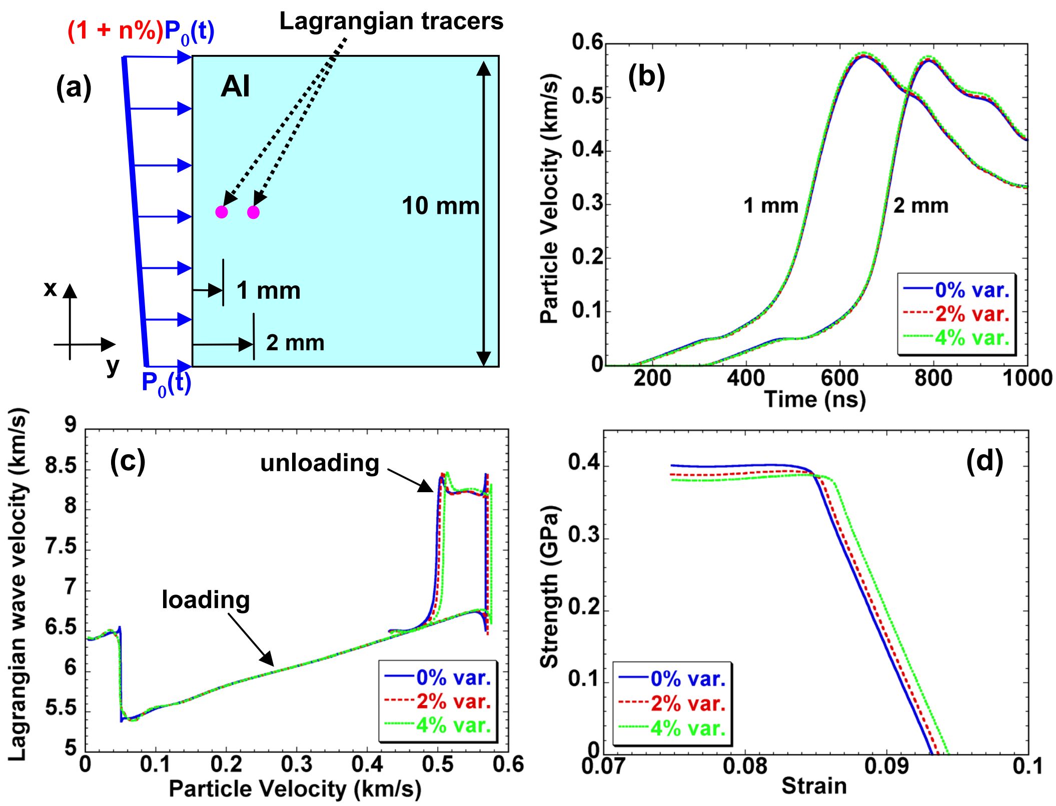

Figure 5.11. (a) 2-D CTH simulations of pressure variation (0%, 2%&4%) across a 10 mm Al sample. (b) Particle speed of Lagrangian tracers at 1 mm and 2 mm locations, ((c) the corresponding Lagrangian wave velocity vs. particle velocity, and (d) strength vs. strain strength vs. strain calculated from the difference between the loading and unloading curves.

Chapter 6

Diagnostics on Veloce

6.1 Air Delay VISAR

The standard approach being used on Veloce to measure particle velocity profiles in ramp loaded samples is as follows. First, the rear side of the load sample (either a free surface or through a transparent window) is illuminated with light from a pulsed laser (Continuum, 532 nm, 5-10 μs, $\sim$ 10 mJ) through a "send" optical fiber ($\sim$ 100 μm in diameter). As the pressure wave propagates through the sample and reaches the reflecting interface, the motion of the sample rear side results in Doppler shifting of the reflected light. The reflected light from the sample is collected by a corresponding "receive" optical fiber ($\sim$ 100 μm in diameter). The Doppler shifted light is relayed via fiber optic cable to an Air Delay VISAR [49, 50], which splits the light into two signals: a reference signal and a time delayed signal.

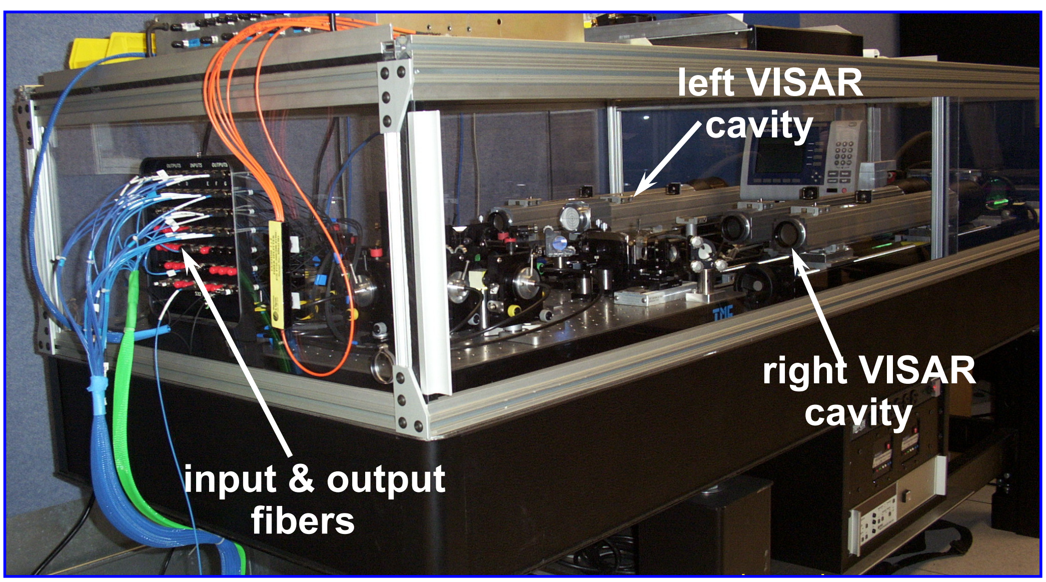

Figure 6.1. Photo of the Air Delay VISAR system.

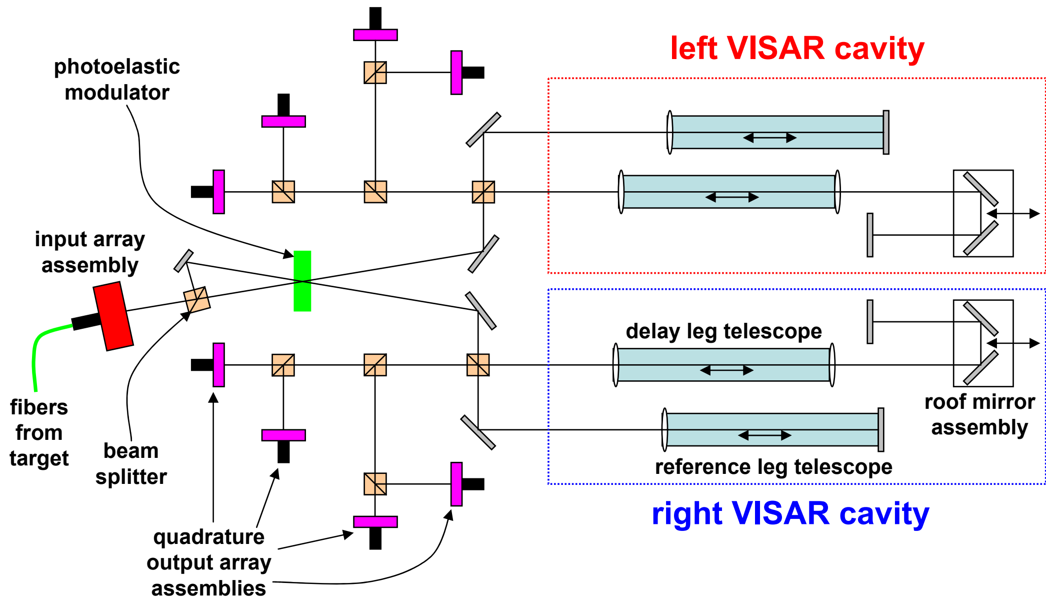

Figure 6.2. Schematic of the Air Delay VISAR.

Figure 6.1 displays the Air Delay VISAR system[1] used on the Veloce machine. In place of the delay etalons used in a conventional VISAR interferometer, a lens system is employed in the Air Delay VISAR interferometer [51] (see Fig. 6.2). This allows for a continuous range in the optical delay from 39.9 mm to 2850 mm (or delay time τ from 0.133 ns to 9.5 ns); this corresponds to continuous variation of the velocity per fringe (VPF) constant from 1000 m/s/f to 14 m/s/f. The reference and delayed signals are combined to form an output signal which is sensed with a fast photodiode (NSTec, Hamamatsu), then digitized and displayed on a digital storage oscilloscope (Tektronix TDS694C, 3 GHz). The center of the circular interference pattern, or "bull's eye", is aligned on the photodiode. When the reflector surface is accelerated, the interfering beams beat together, and the resultant sinusoidal electrical signal is monitored as a function of time using the osilloscope. Together, the recording and digitizing system has a time resolution of ~ 0.5 ns. The use of encoded translation stages results in a total optical path difference uncertainty of ≤ 30 μm, which represents $\leq 0.1\%$ error for a VPF of 1000 m/s/f and proportionately less for lower VPFs. Inclusion of the window optical correction uncertainty ($\sim 0.1\%$) gives a fringe constant uncertainty $\sim 0.15\%$. The velocity uncertainty is stated to be $\leq 0.25\%$. The Air Delay VISAR actually consists of two independent interferometers (referred to as "left" and "right") which allows for each sample locations velocity to be simultaneously measured at two VPFs. Since the dual VPFs velocity measurements have been shown to consistently agree within $\sim 0.3\%$ of each other, the velocity sensitivity of the system has been demonstrated.

[1]The Air Delay VISAR was built for Sandia National Laboratories by NSTec Special Technologies Laboratory.

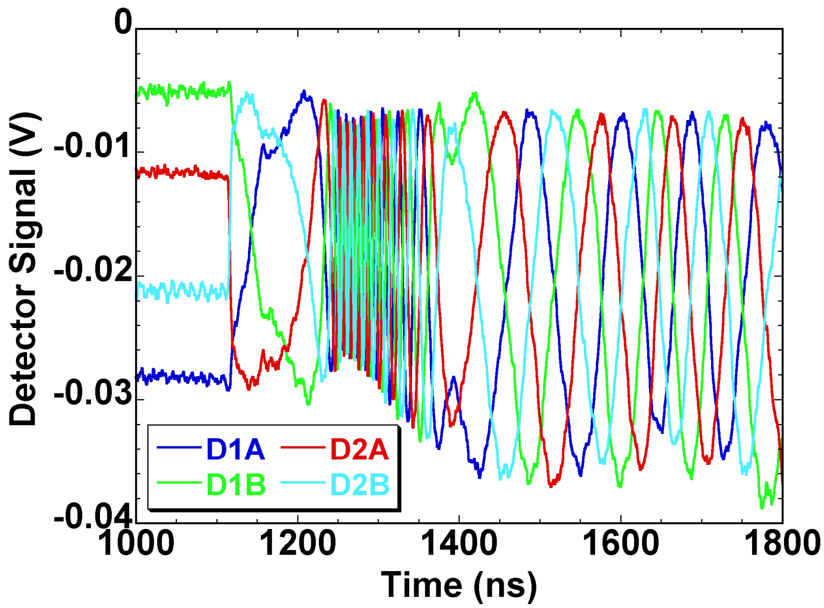

Figure 6.3. Typical quadrature signals obtained from the Air Delay VISAR.

The particle velocity of the sample rear surface is calculated from the fringe shifts of the quadrature output signals of the "push-pull" VISAR (see 6.3) using the PointVISAR analysis package[2] developed by Dolan [52]. The VISAR output signal consists of light that has been superimposed with a time delayed τ version of itself, and its intensity is related to the phase difference $\Phi(t)$ between them,

$$\Phi(t) = \phi(t) - \phi(t - \tau). \tag{6.1}$$

Comparison to the phase difference at each moment in the experiment with an initial reference value occurring in earlier in time by the delay constant yields the fringe shift $F(t)$,

$$F(t) = \frac{\Phi(t) - \Phi(t_i)}{2\pi}. \tag{6.2}$$

The basic interpretation of a VISAR measurement is that changes in velocity correspond to changes in fringe shift. In most situations where events occur significantly slower than the interferometer delay time, the VISAR approximation may be used,

[2] D.H. Dolan, E. Kaltenbach, and K. McCollough, PointVISAR version 2.3.2, Sandia National Laboratories, Albuquerque, NM, 2006.

$$v(t) \approx v_i + KF(t), \tag{6.3}$$

where v_i is the initial velocity and K is the fringe constant (VPF) of the VISAR system. The usual description of K is given as

$$K = \frac{\lambda_0}{2\tau} \frac{1}{(1 + \Delta\nu/\nu)} \frac{1}{(1 + \delta)}, \tag{6.4}$$

where τ is the delay time of the interferometer at the operating wavelength of λ_0, $(1 + \Delta\nu/\nu_0)$ is the correction for the change in index of refraction of the window material. The term $(1 + \delta)$ is the correction term for the frequency dispersion of the etalon in a conventional VISAR, but for the Air Delay VISAR it is neglected.

6.2 Line VISAR

The addition of the Line VISAR diagnostic, or ORVIS (optically recording velocity interferometer system) [53], has expanded the experimental capabilities of the Veloce platform. The schematic of the Line VISAR system is shown in Fig. 6.4, and a photo of the Line VISAR imaging optics mounted onto Veloce is shown in Fig. 6.5. Laser light from a CW laser (Coherent Verdi, 6W, 532 nm)is transported via an optical fiber to the load chamber. Applying the technique of laser light sheet generation [54], the target is efficiently illuminated along a line segment ($\sim$ 2 mm long and $\sim$ 200 μm thick) using a combination of spherical and cylindrical lenses. After passing through a 50/50 beam splitter, the laser light is incident normally onto the target. The collection lens shown in Fig. 6.4 both collects and roughly collimates the diffusely reflected light from the target. As set of relay optics transports the light to the Line VISAR diagnostic which is similar to the previously described Air Delay VISAR diagnostic, except that a high-speed streak camera is used to record interference fringe motion. Additionally, the Line VISAR employs a conventional interferometer with delay etalons.

The accounting of fringe shifts in the Line VISAR system is done in a different manner than in the previous standard VISAR system. Instead of observing the center of a circular interference pattern, the two coherent beams of monochromatic light interfere to produce a parallel set of bright lines at a recombination plane, which is accomplished by rotating the delay leg mirror M2 from its conventional orientation by an angle $\alpha/2$. The frequency of the reflected light from the target is Doppler shifted as the surface moves, which results in a continuously changing wavelegth during the acceleration of the surface. Because of the time delay difference in the two legs of the interferometer, the wavelengths of the two recombined beams are slightly differenct and changing during surface acceration. This produces an apparent motion of the

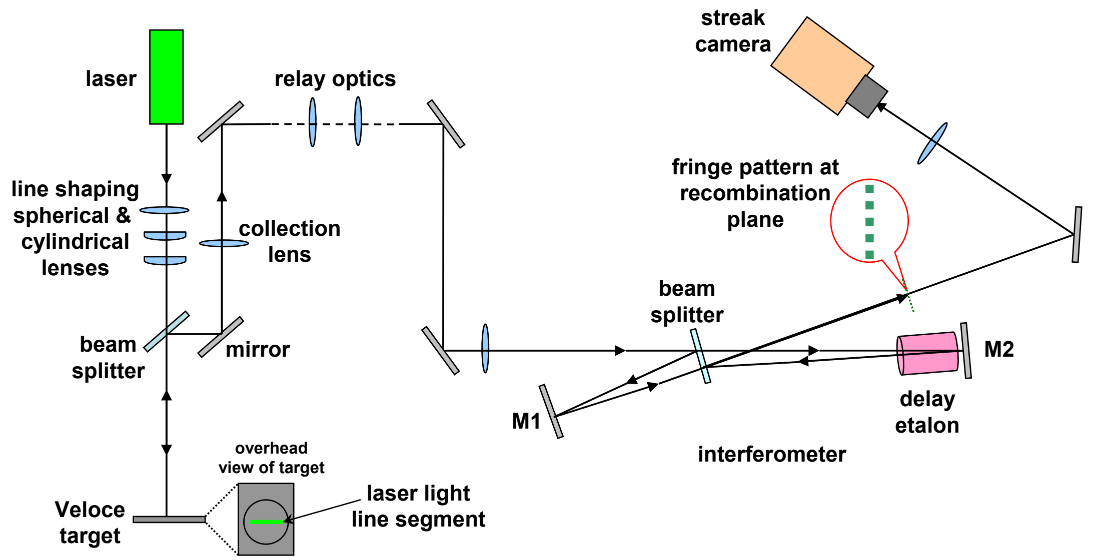

Figure 6.4. Schematic of the Line VISAR system.

fringe pattern in a direction perpendicular to the lines of the fringe pattern (see Fig. 6.6). The velocity of the reflector is linearly proportional to the vertical position of the fringe pattern and the direction of accleration is determined by the direction of the fringe motion. The velocity history is given as

$$v(t - \tau/2) = \frac{\lambda_0 y(t)}{2\tau d(1 + \Delta\nu/\nu_0)/(1 + \delta)}, \tag{6.5}$$

where τ is the temporal difference between the two legs of the interferometer, λ_0 is the laser wavelength, $(1 + \delta)$ is the correction term for the frequency dispersion of the etalon, $(1 + \Delta\nu/\nu_0)$ is the correction for the change in index of refraction of the window material, and d is the fringe spacing on the streak camera slit.

The approach to generate spatially resolved velocity-time profiles from the fringe images is based on the procedured described by Baumung *et al* [55]. At the viewing plane, the parallel interference fringe pattern arises from a well-defined phase relationship between the two legs of the interferometer. This relationship lends itself to treating the moving fringe pattern (upon target acceleration) as a form of quadrature coded signal [56, 57]. In this method, the intensity modulation data are extracted along lines parallel to the time axis of the streak camera image. The intensity-versus-time lineouts are taken at postions corresponding to the fringe center, as well as 1/4, 1/2, and 3/4 the distance to the the center of the neighboring fringe (see Fig. 6.7). This data set may be treated in the same manner as the outputs of the push-pull VISAR system and exported into the previously discussed PointVISAR analysis program (see Fig. 6.8).

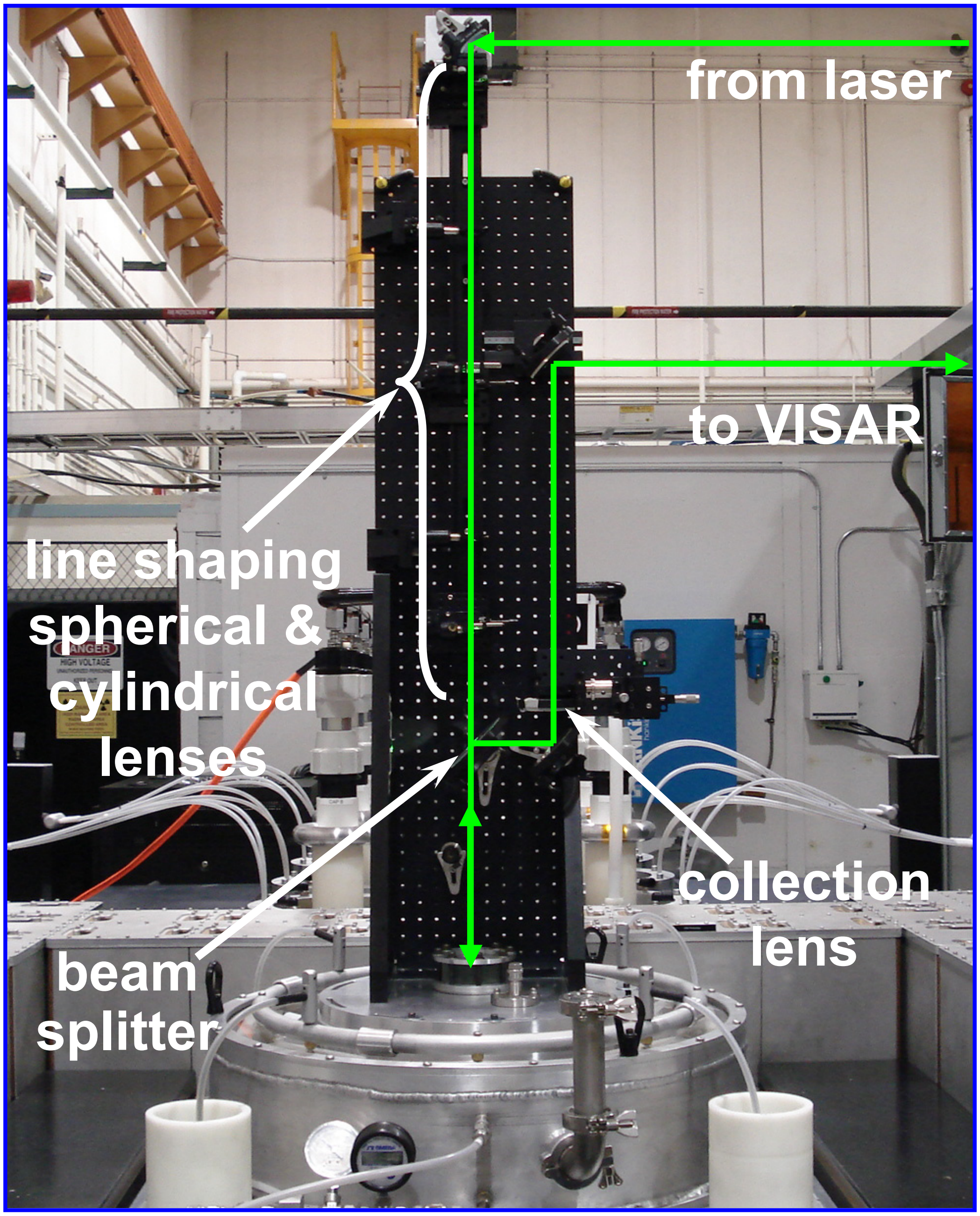

Figure 6.5. Photo of the Line VISAR imaging optics mounted onto Veloce.

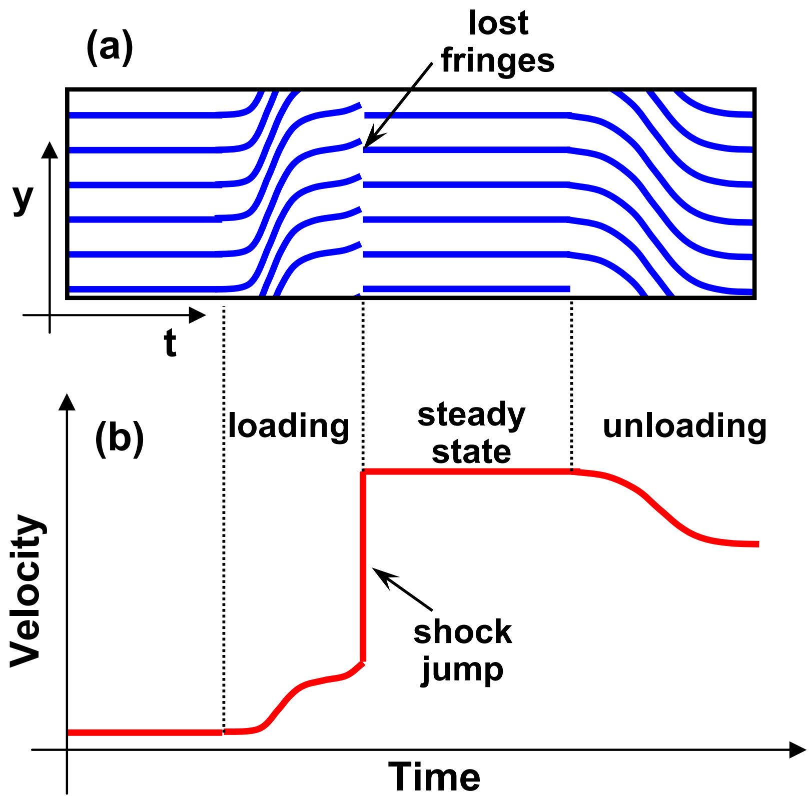

Figure 6.6. (a) Idealized fringe record, and (b) corresponding velocity history.

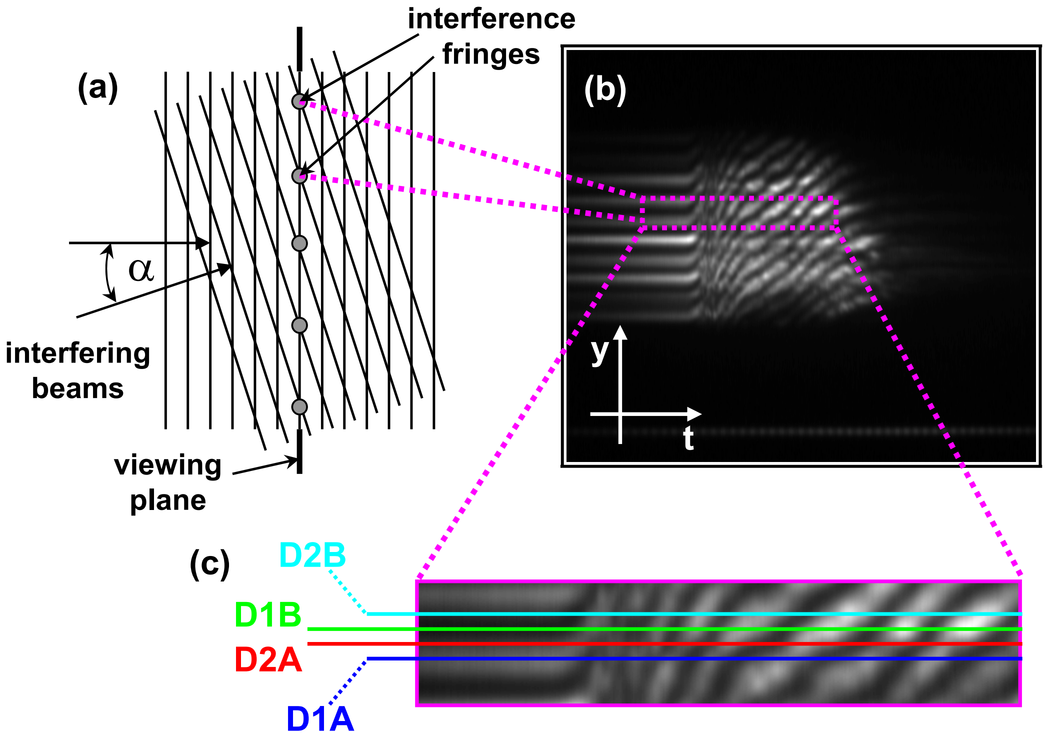

Figure 6.7. (a) Idealized diagram of interference of reference and delay beams, (b) the fringe streak image, (c) relative positions of the lineouts at fringe center, 1/4, 1/2 and 3/4, corresponding to D1A, D2A, D1B and D2B "quadrature signals", respectively.

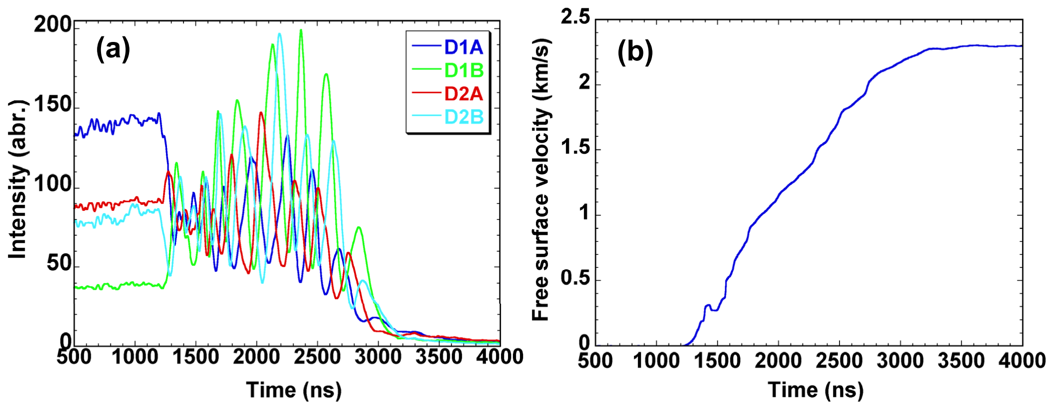

Figure 6.8. (a) The extracted quadrature signals from the line VISAR intensity-versus-time lineouts at the relative positions of fringe center, 1/4, 1/2, and 3/4 the distance to the center of the neighboring fringe , and (b) corresponding velocity history.

Chapter 7

Research on Veloce

Research is in progress to use the Veloce pulser for a wide range of material studies, including EOS, phase transitions, optical properties and material strength with Veloce. Two examples are presented to show the flexibility and quality of data possible. One example is a ramp wave experiment and the other is a shock experiment.

7.1 Strength of aluminum alloys

Recently, several experiments using high-velocity launchers were conducted to study the compressive yield strength of aluminum subjected to high pressure shock loading, unloading and reloading [58, 59]. Aluminum materials of various compositions such as ultrapure aluminum (99.9998% Al), commercially pure aluminum 1060 (99.5% Al), and aluminum alloy 6061-T6 were tested under shock compression over the stress range of 4-22 GPa. The shear stress and shear strength at the shocked state were estimated from reshock and release wave profiles. These data, together with previously reported measurements, ΔY ($\Delta Y = Y_{yield} - Y_{HEL}$), suggest that the increase in strength at shock states increases with applied stress and plastic strain.

To complement the shock data, comparable strength measurements of aluminum under ICE loading have been made using both graded density impactors and the Z accelerator [60]. Additional studies on the strength of various aluminum alloy specimens are being performed on Veloce to further complement previous data [58, 59, 61], and more recent data on ramp loading [60]. Figure 7.1 presents an example of one experiment, in which a set of Al-6061-T0 samples (12 mm diameter, nominally 1.4 and 2.0 mm thick, with LiF windows) were placed on top and bottom modified current contact panels (15 mm wide by 35 mm long). Figure 7.1a displays the velocity histories measured at the Al/LiF interface. The initial elastic precursor is clearly observed propagating ahead of the main plastic wave in both cases. The plastic loading is quite smooth, and occurs over a 250-300 ns risetime. The unloading from peak compression to half peak compression occurs within 300-350 ns. Using the measured velocity profiles, Lagrangian analysis [34] was performed to obtain the Lagrangian wave velocities of the aluminum samples during the ramp loading and unloading (see Fig. 7.1b)). The longitudinal stress and strain were calculated from the conservation relationship of Eq. 7 (see Fig. 7.1b), which is also compared to the Sesame 3700 Al isentrope. The material strength is determined from the difference between the loading and unloading curves for a constant strain level [62]. For a von Mises yield surface, the yield strength in uniaxial tension Y is 0.75 times this difference (see Fig. 7.1d). The complete experimental results of this study on a variety of aluminum alloys is presented in a forthcoming paper [48].

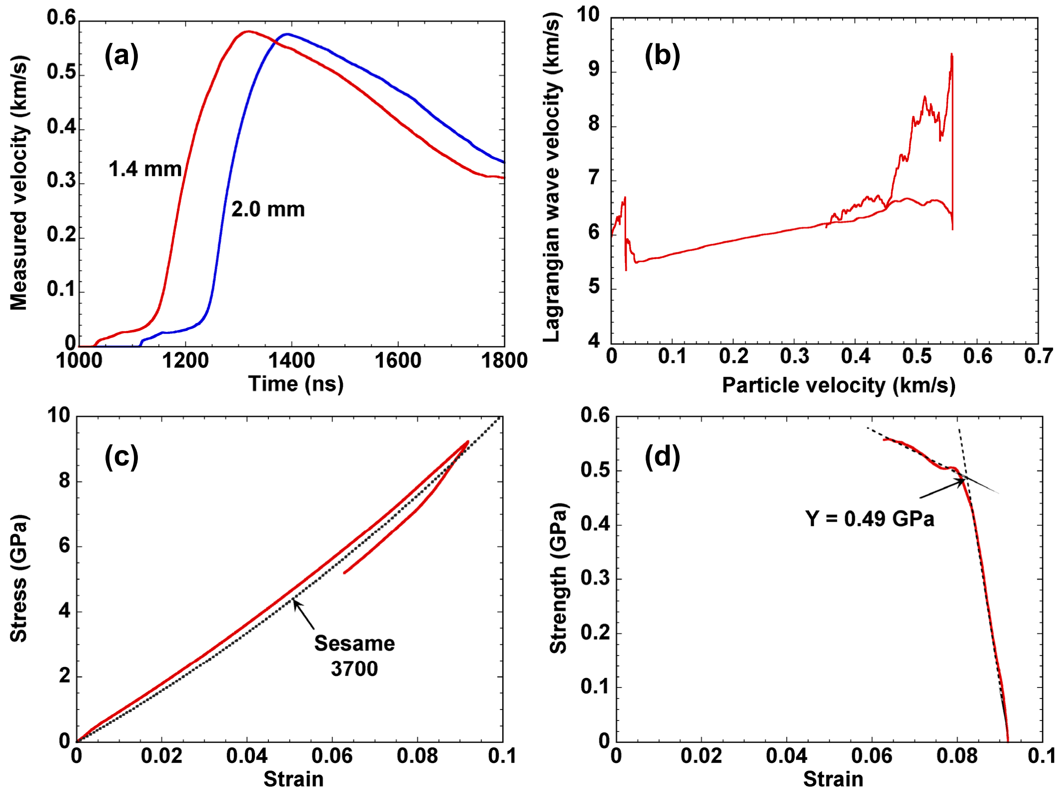

Figure 7.1. ICE loading and unloading of 1.4 and 2.0 mm thick, 12 mm diameter, Al-6061-T0 samples, on 15 × 35 mm modified current contact 1100 Al panels. (a) The measured Al/Lif interface velocity profiles, (b) the Lagrangian wave velocity vs the particle velocity of the Al, (c) the stress vs. strain curve along with the Sesame 3700 Al isentrope, and (d) the material strength evaluated from the loading and unloading curves.

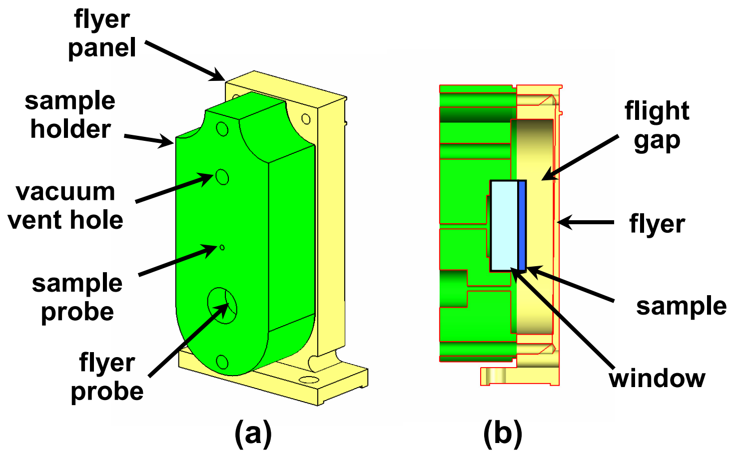

Figure 7.2. (a) The assembled flyer panel and sample holder, and (b) the cross-section view with a sample/window in place.

7.2 Launching of flyer plates for shock compression experiments

The pulsed power ramp loading technique can also be utilized for launching flyer plates to high velocities for use in shock compression research [26, 27, 28]. In this application, the load configuration is modified slightly from the ramp loading arrangement. Namely, the samples are taken off the load panels and situated at a flight gap distance of 3-5 mm away from the panels. The impulsive pressure produced by ramp loading provides sufficient momentum to launch the load panels across the gap at a high velocity and impact the load samples [27, 39, 28].

Fig. 7.2 shows the flyer panel and sample holder used for flyer plate experiments. The flyer panel is similar in dimensions to typical load panels except the floor thickness is slightly thinner ($\sim$ 1 mm) to allow for increase flyer velocity. At the center of the sample holder is a cavity where the sample/window is deposited and glued in place. Two probe holes are drilled into the holder, one at the center sample location, and another below the sample. The latter probe tracks the flyer plate as it travels across the flight gap, while the former measures the shock wave propagating through the sample. As previously discussed, the load region of Veloce cannot support a reasonable vacuum environment. Instead, the interior of the load region is filled with N_2 gas at a pressure of $\sim$ 1 atm. However, gas within the flight gap is unwanted for several reasons. First, as the flyer plate travels across the flight gap, the gas will be compressed, heat up and ablate the flyer plate. Second, a precursor bow wave will hit the sample before the flyer plate can impact it. Thus, an additional larger vacuum vent hole is drilled near the top of the sample holder. The sample

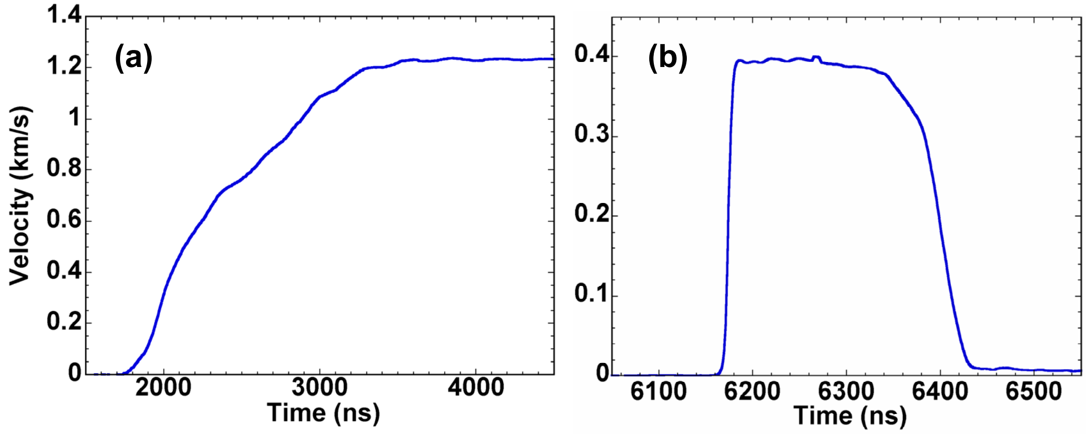

Figure 7.3. (a) The measured free surface velocity of a 1 mm thick flyer panel. (b) The measured particle velocity of a shocked sapphire sample (c-axis, 0.5 mm) with a sapphire window (c-axis, 5 mm thick).

holder is placed on top of the panel with a lining of glue at the edges to seal in the flight gap, which is then evacuated to a pressure of $\sim$ 30 mTorr. Fig. 7.3a shows the measured free surface velocities for 1 mm thick flyer panels. The flyer is smoothly accelerated within $\sim$ 1800 ns up to a constant final velocity. After traversing the flight gap, the flyer impacts a sapphire sample (c-axis, 0.5 mm thick) with a sapphire window (c-axis, 5 mm thick). At the sample/window interface, a thin Al film (0.25 μm thick) is deposited to allow the particle velocity of the shocked sapphire sample to be measured, as shown in Fig. 7.3b. A steady shock state in the sapphire is observed for $\sim$ 160 ns before it is extinguished by the release wave propagating from the far side of the flyer plate. During acceleration, melting of the flyer is caused by Joule heating of the flyer material in association with diffusion of the drive magnetic field into the flyer panel [28]. Compared to a fully intact flyer, the resulting release wave of the ablated layer reduces the shock duration by $\sim$ 25%.

The spatial nonuniformities in the magnetic field, discussed in the previous section, have a direct affect on the planarity of the flyer panel. From the simulations (see Fig. 5.4c), the magnetic field variation laterally across the panel within the diameter of a sample is $\sim$ 0.2%, or $\sim$ 0.4% pressure variation. Thus, the flyer is fairly planar within its central region over a diameter of 3 mm. However, because of the formerly described nonuniformity along the panel, a vertical tilt on the flyer would be evident. Initial measurements on the flyer panel have observed tilt angles upon impact with the sample of $\sim$ 3 mrads. Through implementation of the aforementioned improvements to decrease the panel drive pressure nonuniformities, the flyer tilt should be reduced likewise.

Chapter 8

Discussion and Conclusions

With the development of the Veloce compact strip-line pulsed power generator, research on isentropic compression of materials is now more accessible to the scientific community. While the pressures (5-20 GPa) achievable on it are presently considerably lower than those attained at the Z accelerator, Veloce does fill an experimental niche needed to explore the response of materials subjected to shockless loading at lower stresses and strain rates of 10^6 - 10^7 /s. Experiments on the pulser must be designed to balance peak pressures attainable with lateral edge effects resulting from the rather long loading times produced in the pulser. In order to obtain accurate dynamic material response data, careful consideration of these competing requirements must be made in the design, preparation and configuration of the load samples and panels.

The most important issue investigated in the present study, both experimentally and through 3-D MHD simulations, was the inherent nonuniformity observed in the ramp loading of the samples. Ideally, for completely uniform loading, samples should be situated on an infinite or at least very large surface. Unfortunately, such a situation is not experimentally viable. With a finite available current, the load surface must be restricted in size to achieve a high enough current density to create the desired large magnetic pressures. 3-D MHD simulations were performed on a variety of load panel designs involving different panel lengths and widths, notches, tapering of panels, and modified current contacts. Although the insertion of notches near the base of the panels did resolve the pressure nonuniformity for the lower section of the panel, the upper current contact section of the panel remained unaffected. The application of panel tapering, with the panel width increasing from the panel base to the current contact, was effective in almost completely eliminating the pressure gradient along the panel, but at a significant cost of 10% in loading pressure. Whereas the panel design with the modified current contacts was shown to diminish the nonuniformity due to the current contact, and with only a minor loss of loading pressure. Implementing these designs on future load panels should minimize the loading nonuniformity.

The pulser has been demonstrated to produce smooth, continuous isentropic loading of samples up to 17 mm in diameter and 2.5 mm in thickness. In addition, high quality data for measuring the dynamic strength of aluminum alloys has been obtained. Furthermore, the launching of flyer plates for shock compression experiments has also been demonstrated on Veloce. Upcoming isentropic loading campaigns on Veloce include studies of the dynamic strength of high impedance materials such as vanadium and tantalum, the high-pressure compression mechanical and optical response of laser window materials (LiF, NaCl, sapphire, etc.), and the chemical phase transitions occurring in energetic materials.

References

[1] R. G. McQueen, S. P. Marsh, J. W. Taylor, J. N. Fritz, and W. J. Carter, "The equation of state of solids from shock wave studies," in *High-Velocity Impact Phenomena* (R. Kinslow, ed.), (New York), pp. 249–417, Academic Press, 1970.

[2] R. J. Trainor, J. W. Shaner, J. M. Auerbach, and N. C. Holmes, "Ultrahigh-pressure laser-driven shock-wave experiments in aluminum," *Physical Review Letters*, vol. 42, no. 17, pp. 1154–1157, 1979.

[3] A. C. Mitchell and W. J. Nellis, "Shock compression of aluminum, copper, and tantalum," *Journal of Applied Physics*, vol. 52, no. 5, pp. 3363–3374, 1981.

[4] C. E. R. III, "Shock-wave experiments at three-fold compression," *Physical Review A (General Physics)*, vol. 29, no. 3, pp. 1391–1402, 1984.

[5] L. M. Barker and R. E. Hollenbach, "Shock-wave studies of PMMA, Fused Silica, and Sapphire," *Journal of Applied Physics*, vol. 41, no. 10, pp. 4208–4226, 1970.

[6] W. B. Benedick and J. R. Asay, "High-pressure ramp wave generators," *Bull. Amer. Phys. Soc.*, vol. 21, p. 1298, 1976.

[7] L. M. Barker, "High-pressure quasi-isentropic impact experiments," in *Shock Waves in Condensed Matter-1983* (J. R. Asay and R. A. Graham and G. K. Straub, ed.), (New York), pp. 217–224, Elsevier, 1984.

[8] J. H. Nguyen, D. Orlikowski, F. H. Streitz, J. A. Moriarty, and N. C. Holmes, "High-pressure tailored compression: Controlled thermodynamic paths," *Journal of Applied Physics*, vol. 100, no. 2, p. 023508, 2006.

[9] J. Edwards, K. T. Lorenz, B. A. Remington, S. Pollaine, J. Colvin, D. Braun, B. F. Lasinski, D. Reisman, J. M. McNaney, J. A. Greenough, R. Wallace, H. Louis, and D. Kalantar, "Laser-driven plasma loader for shockless compression and acceleration of samples in the solid state," *Physical Review Letters*, vol. 92, no. 7, p. 075002, 2004.

[10] R. F. Smith, J. H. Eggert, A. Jankowski, P. M. Celliers, M. J. Edwards, Y. M. Gupta, J. R. Asay, and G. W. Collins, "Stiff response of aluminum under ultrafast shockless compression to 110 GPa," *Physical Review Letters*, vol. 98, no. 6, p. 065701, 2007.

[11] J. F. Barnes, P. J. Blewett, R. G. McQueen, K. A. Meyer, and D. Venable, "Taylor instability in solids," *Journal of Applied Physics*, vol. 45, no. 2, pp. 727–732, 1974.

[12] D. C. Swift and R. P. Johnson, "Quasi-isentropic compression by ablative laser loading: Response of materials to dynamic loading on nanosecond time scales," *Physical Review E (Statistical, Nonlinear, and Soft Matter Physics)*, vol. 71, no. 6, p. 066401, 2005.

[13] J. R. Asay, "Isentropic compression experiments on the Z Accelerator," in *Shock Compression of Condensed Matter-1999* (M. D. Furnish and L. C. Chhabildas and R. S. Hixson, ed.), (New York), p. 261, AIP, 2000.

[14] C. A. Hall, "Isentropic compression experiments on the Sandia Z Accelerator," *Physics of Plasmas*, vol. 7, pp. 2069–2075, 2000.

[15] J. Asay and M. Knudson, "Use of pulsed magnetic fields for quasi-isentropic compression experiments," in *High-Pressure Shock Compression of Solids VIII: The Science and Technology of High-Velocity Impact* (L. Chhabildas, L. Davison, and Y. Horie, eds.), p. 329, 2005.

[16] R. B. Spielman, C. Deeney, G. A. Chandler, M. R. Douglas, D. L. Fehl, M. K. Matzen, D. H. McDaniel, T. J. Nash, J. L. Porter, T. W. L. Sanford, J. F. Seamen, W. A. Stygar, K. W. Struve, S. P. Breeze, J. S. McGurn, J. A. Torres, D. M. Zagar, T. L. Gilliland, D. O. Jobe, J. L. McKenney, R. C. Mock, M. Vargas, T. Wagoner, and D. L. Peterson, "Tungsten wire-array Z-pinch experiments at 200 TW and 2 MJ," *Physics of Plasmas*, vol. 5, pp. 2105–2111, 1998.

[17] C. A. Hall, J. R. Asay, M. D. Knudson, D. B. Hayes, R. L. Lemke, J. P. Davis, and C. Deeney, "Recent advances in quasi-isentropic compression experiments (ICE) on the Sandia Z Accelerator," in *Shock Compression of Condensed Matter* (M. D. Furnish, Y. Horie, and N. N. Thadhani, eds.), vol. 620 of *American Institute of Physics Conference Series*, pp. 1163–1168, 2002.

[18] D. B. Reisman, A. Toor, R. C. Cauble, C. A. Hall, J. R. Asay, M. D. Knudson, and M. D. Furnish, "Magnetically driven isentropic compression experiments on the Z accelerator," *Journal of Applied Physics*, vol. 89, pp. 1625–1633, 2001.

[19] C. A. Hall, J. R. Asay, M. D. Knudson, W. A. Stygar, R. B. Spielman, T. D. Pointon, D. B. Reisman, A. Toor, and R. C. Cauble, "Experimental configuration for isentropic compression of solids using pulsed magnetic loading," *Review of Scientific Instruments*, vol. 72, pp. 3587–3595, 2001.

[20] J.-P. Davis, C. Deeney, M. D. Knudson, R. W. Lemke, T. D. Pointon, and D. E. Bliss, "Magnetically driven isentropic compression to multimegabar pressures using shaped current pulses on the Z accelerator," *Physics of Plasmas*, vol. 12, p. 6310, 2005.

[21] J.-P. Davis, "Experimental measurement of the principal isentrope for aluminum 6061-T6 to 240 GPa," *Journal of Applied Physics*, vol. 99, no. 10, p. 103512, 2006.

[22] D. Hayes, "Unsteady compression waves in interferometer windows," *Journal of Applied Physics*, vol. 89, pp. 6484–6486, 2001.

[23] D. B. Hayes, C. A. Hall, J. R. Asay, and M. D. Knudson, "Continuous index of refraction measurements to 20 GPa in Z-cut sapphire," *Journal of Applied Physics*, vol. 94, pp. 2331–2336, 2003.

[24] J.-P. Davis and D. B. Hayes, "Isentropic compression experiments on dynamic solidification in tin," in *American Institute of Physics Conference Series*, vol. 706 of *American Institute of Physics Conference Series*, pp. 163–166, 2004.

[25] J. L. Ding and J. R. Asay, "Material characterization with ramp wave experiments," *Journal of Applied Physics*, vol. 101, no. 7, p. 073517, 2007.

[26] C. A. Hall, M. D. Knudson, J. R. Asay, and B. Oliver, "High velocity flyer plate launch capability on the Sandia Z accelerator," *Int. J. Impact Engineering*, vol. 26, p. 275, 2002.

[27] M. D. Knudson, R. W. Lemke, D. B. Hayes, C. A. Hall, C. Deeney, and J. R. Asay, "Near-absolute Hugoniot measurements in aluminum to 500 GPa using a magnetically accelerated flyer plate technique," *Journal of Applied Physics*, vol. 94, pp. 4420–4431, 2003.

[28] R. W. Lemke, M. D. Knudson, D. E. Bliss, K. Cochrane, J.-P. Davis, A. A. Giunta, H. C. Harjes, and S. A. Slutz, "Magnetically accelerated, ultrahigh velocity flyer plates for shock wave experiments," *Journal of Applied Physics*, vol. 98, no. 7, p. 073530, 2005.

[29] P. L. Hereil, F. Lassalle, and G. Avrillaud, "GEPI : An ICE generator for dynamic material characterisation and hypervelocity impact," in *American Institute of Physics Conference Series*, vol. 706 of *American Institute of Physics Conference Series*, pp. 1209–1212, 2004.

[30] G. Avrillaud, L. Courtois, J. Guerre, P. L. Hereil, F. Lassalle, F. Bayol, P. LEplattenier, B. Kovalchuk, E. Kumpjak, N. Zoi, and A. Kim, "GEPI: a compact pulsed power driver for isentropic compression experiments and for non shocked high velocity flyer plates," in *14th IEEE International Pulsed Power Conference*, vol. 2 of *American Institute of Physics Conference Series*, pp. 913–916, 2003.

[31] J. Osher, R. Gathers, H. Chau, R. Lee, R. Pomykal, and R. Weingart, "Hypervelocity acceleration and impact experiments with the LLNL electric guns," *Int. J. Impact Engng.*, vol. 10, p. 439, 1990.

[32] L. Davison and R. A. Graham, "Shock compression of solids," *Physics Report*, vol. 55, pp. 255–379, 1979.

[33] J. R. Asay and G. I. Kerley, "The response of materials to dynamic loading," *Int. J. Impact Engng*, vol. 5, pp. 69–99, 1987.

[34] J. B. Aidun and Y. M. Gupta, "Analysis of Lagrangian gauge measurements of simple and nonsimple plane waves," *Journal of Applied Physics*, vol. 69, no. 10, pp. 6998–7014, 1991.

[35] L. Chhabildas and L. M. Barker, "Dynamic quasi-isentropic compression of tungsten," in *Shock Waves in Condensed Matter-1987* (S.C. Schmidt and N.C. Holmes, ed.), (New York), p. 111, Elsevier, 1988.

[36] J. M. Meeks and J. D. Craggs, *Electrical Breakdown of Gases.* New York, USA: John Wiley & Sons, 1978.

[37] S. K. Carroll, R. R. Drake, D. M. Hensinger, C. B. Luchini, S. V. Petney, J. Robbins, A. C. Robinson, R. M. Summers, T. E. Voth, M. K. Wong, T. A. Brunner, C. J. Garasi, T. A. Haill, and T. A. Mehlhorn, "ALEGRA: version 4.6," Technical report SAND2004-6541, Sandia National Laboratories, Albuquerque, New Mexico 87185, Jan. 2004.

[38] T. Haill, T. Mehlhorn, J. Asay, Y. Gupta, R. Lawrence, C. Bakeman, and J. Follett, "A feasibility study for a fragment-producing chemical-electrical launcher," in *Proc. 17th IEEE Int. Pulsed Power Conf. 2007*, 2007. (submitted).

[39] R. W. Lemke, M. D. Knudson, J.-P. Davis, D. Bliss, and H. Harjes, "Self-consistent, 2D magneto-hydrodynamic simulations of magnetically driven flyer plate experiments on the Z-Machine," in *Shock Compression of Condensed Matter* (M. D. Furnish, Y. Gupta, and J. W. Forbes, eds.), vol. 706 of *American Institute of Physics Conference Series*, pp. 1175–1180, 2004.

[40] G. Kerley, "CTH reference manual: the equation of state package," Technical report SAND98-0947, Sandia National Laboratories, Albuquerque, New Mexico 87185, Apr. 1998.

[41] G. I. Kerley, "Theoretical equation of state for aluminum," *Int. J. Impact Engng*, vol. 5, p. 441, 1987.

[42] J. Chakrabarty, *Theory of plasticity.* New York, USA: McGraw-Hill, 1987.

[43] D. Steinberg, "Equation of state and strength properties of selected materials," LLNL Technical report UCRL-MA-106439, Change 1, Lawrence Livermore National Laboratory, Livermore, CA, Feb. 1991.

[44] M. P. Desjarlais, "Practical improvements to the Lee-More Conductivity near the metal-insulator transition," *Contrib. Plasma Phys.*, vol. 41, no. 2, pp. 267–270, 2001.

[45] M. P. Desjarlais, J. D. Kress, and L. A. Collins, "Electrical conductivity for warm, dense aluminum plasmas and liquids," *Phys. Rev. E*, vol. 66, no. 2, p. 025401, 2002.

[46] J. M. McGlaun, S. L. Thompson, and M. Elrick, "CTH: a Three-Dimensional Shock Wave Physics Code," *Int. J. Impact Engng*, vol. 10, pp. 351–360, 1990.

[47] M. R. Baer, C. A. Hall, R. L. Gustavsen, D. E. Hooks, and S. A. Sheffield, "Isentropic loading experiments of a plastic bonded explosive and constituents," *Journal of Applied Physics*, vol. 101, no. 3, p. 034906, 2007.

[48] J. R. Asay, T. Ao, J.-P. Davis, M. Knudson, C. Hall, and G. Gray, "Effect of initial properties on the flow strength of aluminum during quasi-isentropic compression," *Journal of Applied Physics*, 2007. (submitted).

[49] L. M. Barker and R. E. Hollenbach, "Laser interferometer for measuring high velocities of any reflecting surface," *Journal of Applied Physics*, vol. 43, no. 11, pp. 4669–4675, 1972.

[50] W. Hemsing, "Velocity sensing interferometer (VISAR) modification," *Review of Scientific Instruments*, vol. 50, no. 1, pp. 73–78, 1979.

[51] B. Amery, "Wide range velocity interferometer," in *6th Symposium on Detonation*, AC-R-22-1, Office of Naval Research, Dept. of the Navy, Arlington, VA, p. 673, 1976.

[52] D. Dolan, "Foundations of VISAR analysis," Technical report SAND2006-1950, Sandia National Laboratories, Albuquerque, New Mexico 87185, June 2006.

[53] D. D. Bloomquist and S. A. Sheffield, "Optically recording interferometer for velocity measurements with subnanosecond resolution," *Journal of Applied Physics*, vol. 54, pp. 1717–1722, 1983.

[54] G. Diemunsch and J. P. Prenel, "A compact light sheet generator for flow visualizations," *Opt. Laser Technol.*, vol. 19, pp. 141–144, 1987.

[55] K. Baumung, J. Singer, S. V. Razorenov, and A. V. Utkin, "Hydrodynamic proton beam-target interaction experiments using an improved line-imaging velocimeter," in *Shock Compression of Condensed Matter* (S. C. Schmidt and W. C. Tao, eds.), vol. 370, pp. 1015–1018, AIP, 1996.

[56] W. M. Trott, M. R. Baer, J. N. C. neda, L. C. Chhabildas, and J. R. Asay, "Investigation of the mesoscopic scale response of low-density pressings of granular sugar under impact," *Journal of Applied Physics*, vol. 101, no. 2, p. 024917, 2007.

[57] W. M. Trott, J. N. Castaneda, J. J. O'Hare, M. B. Baer, L. C. Chhabildasa, M. D. Knudson, J. P. Davis, and J. R. Asay, "Dispersive velocity measurements in heterogeneous materials," Technical report SAND2000-3082, Sandia National Laboratories, Albuquerque, New Mexico 87185, Dec. 2000.

[58] H. Huang and J. R. Asay, "Compressive strength measurements in aluminum for shock compression over the stress range of 4–22 GPa," *Journal of Applied Physics*, vol. 98, no. 3, p. 033524, 2005.

[59] H. Huang and J. R. Asay, "Reshock response of shock deformed aluminum," *Journal of Applied Physics*, vol. 100, no. 4, p. 043514, 2006.

[60] T. J. Vogler, T. Ao, and J. Asay, "High-pressure strength of aluminum under quasi-isentropic loading," *Int. J. Plasticity*, 2007. (submitted).

[61] J. Asay and L. Chhabildas, "Shock waves and high-strain-rate phenomena in metals," in *Shock Waves and High Strain-Rate Phenomena in Metals: Concepts and Applications* (M.A. Meyer and L.E. Murr, ed.), (New York), p. 417, Plenum, 1981.

[62] J. R. Asay and J. Lipkin, "A self-consistent technique for estimating the dynamic yield strength of a shock-loaded material," *Journal of Applied Physics*, vol. 49, no. 7, pp. 4242–4247, 1978.

DISTRIBUTION:

1 L.C. Chhabildas
Air Force Research Laboratory/MNMW
101 West Eglin Blvd., Suite 135
Eglin Air Force Base, FL 32542

1 D. Dandekar
AMSRL-WM-TD
Army Research Laboratory
Aberdeen Proving Ground, MD 21005-5066

1 C. Deeney
Director, Office of Defense Science
National Nuclear Security Administration
U.S. Department of Energy
NA-11/Forrestal Building
1000 Independence Ave., S.W.
Washington, DC 20585

4 Washington State University
Institute for Shock Physics
P.O. Box 642814
Pullman, WA 99164-2814
Attn: C. Bakeman
Y.M Gupta
T. Jaglinksi
C.S. Yoo

6 Los Alamos National Laboratory
P.O. Box 1663
Los Alamos, NM 87545
Attn: W.V. Anderson
R.L. Gustavsen
G.T. Gray, III
R.S. Hixson
B.J. Jensen
D.L. Preston
P.A. Rigg

14 Lawrence Livermore National Laboratory
7000 East Ave.
Livermore, CA 94450
Attn: K.S. Budil
R.C. Cauble
G.W. Collins
M.J. Edwards
J.H. Eggert
N.C. Holmes
J.O. Kane
M.A. Linquist
J.H. Nguyen
D.B. Reisman
B.A. Remington
R.F. Smith
D.C. Swift
K.S. Vandersall

1 G. Avrillaud
International Technologies for High Pulsed Power
Drele, 46500 Thegra
FRANCE

1 Steve Rothman
AWE Aldermaston
Bldg. E1
Reading, RG7 4PR
UNITED KINGDOM

1 MS 0378 E.O. Strack, 1431

1 MS 0382 E.S. Hertel, 1545

1 MS 0826 W.M. Trott, 1512

1 MS 0836 M.R. Baer, 1500

20 MS 1106 T. Ao, 1646

1 MS 1152 S. Chantrenne, 1646

1	MS 1152	S.F. Glover, 1654
1	MS 1152	K.W. Reed, 1654
1	MS 1159	S.C. Jones, 1344
5	MS 1168	C.A. Hall, 1646
1	MS 1168	M.D. Furnish, 1647
2	MS 1181	J.R. Asay, 1646
1	MS 1181	C.S. Alexander, 1647
1	MS 1181	J.-P. Davis, 1646
1	MS 1181	D.H. Dolan, 1646
1	MS 1181	S.A. Grine-Jones, 1646
5	MS 1181	R.J. Hickman, 1646
1	MS 1181	M.D. Knudson, 1646
1	MS 1181	T.A. Mehlhorn, 1640
1	MS 1181	S. Root, 1646
1	MS 1181	L.X. Schneider, 1650
1	MS 1181	A.W. Shay, 1646
1	MS 1181	T.J. Vogler, 1647
1	MS 1181	M.D. Willis, 1646
1	MS 1181	J.L. Wise, 1646
1	MS 1186	M.P. Desjarlais, 1640
1	MS 1186	R.W. Lemke, 1641
1	MS 1186	T.A. Haill, 1641
1	MS 1190	M.K. Matzen, 1600

1 MS 1322 J.B. Aidun, 1435

1 MS 0899 Technical Library, 9536 (electronic copy)

Sandia National Laboratories